Original Article

Application of the Maximum Flow–Minimum Cut Algorithm to Segmentation and Clustering of Materials Datasets

Alexander F. Brust[1], Eric J. Payton[2], Toren J. Hobbs[1] and Stephen R. Niezgoda[1,3]*

[1]Department of Materials Science and Engineering, The Ohio State University, Columbus, OH 43210, USA; [2]Air Force Research Laboratory, Materials and Manufacturing Directorate, Dayton, OH 45433, USA and [3]Department of Mechanical and Aerospace Engineering, The Ohio State University, Columbus, OH 43210, USA

Abstract

Problems involving image segmentation, atomic cluster identification, segmentation of microstructure constituents in images and austenite reconstruction have seen various approaches attempt to solve them with mixed results. No single computational technique has been able to effectively tackle these problems due to the vast differences between them. We propose the application of graph cutting as a versatile technique that can provide solutions to numerous materials data analysis problems. This can be attributed to its configuration flexibility coupled with the ability to handle noisy experimental data. Implementation of a *Bayesian statistical* approach allows for the *prior* information, based on experimental results and already ingrained within nodes, to drive the expected solutions. This way, nodes within the graph can be grouped together with similar, neighboring nodes that are then assigned to a specific system with respect to calculated likelihoods. Associating probabilities with potential solutions and states of the system allows for quantitative, stochastic analysis. The promising, robust results for each problem indicate the potential usefulness of the technique so long as a network of nodes can be effectively established within the model system.

Key words: atomic clustering, Bayesian statistics, graph cutting, segmentation

(Received 13 September 2018; revised 9 May 2019; accepted 21 May 2019)

Introduction

The analysis and post-processing of materials characterization datasets are often more challenging and time-consuming than the acquisition of the raw data (Duval et al., 2014). For example, image segmentation, or the problem of automatically separating and classifying features of interest from the background, is a common analysis task where it is trivial to complete by the human eye but often difficult for a computer to reliably and repeatably accomplish. Consider the problem of segmenting a micrograph of a material containing multiple thermodynamic phases: A naïve approach for segmentation consists of identifying a threshold on the intensity which will classify the image pixels by phase. More often than not, this approach will fail due to insufficient contrast between the phases, uneven illumination of the sample, surface topology of the sample, noise in the image, etc (McInerney & Terzopoulos, 1999; Despotović et al., 2010; Zhu et al., 2013). Denoising, or some other form of cleanup, will oftentimes be applied to the data in order to remove some of these artifacts before or after segmentation; however, this approach can be resource intensive, is not easily automated, and may only be partially successful (Preethi & Narmadha, 2012; Soni et al., 2014).

Common analysis procedures such as segmentation and clustering are particular examples of a larger class of inverse imaging problems (Otsu, 1979; Lloyd, 1982). As in the segmentation example above, these inverse problems are often ill-posed without a unique solution (i.e. for the segmentation problem, the pixels cannot be assigned to a class based solely on their intensity). Instead, we need to regularize the problem by including some additional information. Oftentimes, this involves basic physical considerations, such as a high interfacial energy between two phases, making it more likely to result in smoother, shorter interfaces, and compact regions of secondary phases. Similar physical intuition can be applied to other imaging modalities as well. For example, in electron backscatter diffraction (EBSD) datasets, it might be reasonable to assume that the lattice orientation changes slowly across grain and the dataset can be approximated by a piecewise smooth orientation field, where sharp transitions in orientation occur only at grain boundaries.

As imaging techniques and data-collection become faster and more automated, it is important to simultaneously automate the data analysis. In microscopy, the application of advanced techniques such as generalized Markov Random Field (MRF) techniques (Mondal et al., 2007; Lee & Han, 2013) to regularize segmentation based with an interfacial energy penalty is steadily becoming more popular. The goal of the present work is to extend these ideas and to introduce a general computational framework which common imaging and data analysis inverse problems can be easily and intuitively formulated, resulting in quick, efficient solutions.

Graph cutting algorithms are a common technique in the area of low-level computer vision for solving problems such as image correspondence (feature registration) from multiple cameras,

*Author for correspondence: Stephen R. Niezgoda, E-mail: niezgoda.6@osu.edu

feature extraction, and model-based smoothing and filtering (Veksler, 2003; Wills et al., 2003; Imre et al., 2010; Bae et al., 2011; Iyer et al., 2017), all of which can be formulated as an energy minimization problem (Greig et al., 1989; Boykov & Veksler, 2006). Graph cutting is gaining traction for feature segmentation in a few biological imaging applications. In general, its utility has been demonstrated in applications involving segmentation of predefined shapes, like ellipses, for features with good contrast against the backgrounds, such as cells, chromosomes, and protein segmentation and identification (Leskó et al., 2010; Beheshti et al., 2015; Soubies et al., 2015), as well as analysis of bone tissue images to quantify the blood permeability of bone marrow (Shigeta et al., 2014).

Despite its maturity in computer vision applications, graph cutting has not found wide application within the materials science community. One notable exception is the work of Waggoner et al., where a graph-cut formulation was successfully applied to segment grains from 3D serial sectioned polycrystalline datasets by propagating features from a template or one segmented image to the others in the stack (Waggoner et al., 2013, 2014). In the present work, we present a new framework which is particularly suited to clustering and phase segmentation of microscopy images and multi-modal materials datasets.

Graph cutting relies on recasting the dataset to be operated on as a graph, or network, with individual data points redefined as nodes and relationships between the data points acting as edges or connections between the nodes. For example, in terms of image segmentation, the pixels of an image would be represented as nodes in the graph which might be connected to all neighboring pixels by graph edges. The goal of the graph cut approach is to separate the graph into two disjoint sets while minimizing the energy of the cut (i.e. the number of cut edges and the penalty associated with cutting each edge). As will be described below, the penalty associated with cutting each edge does not need to be uniform but can be assigned based on the particular regularization problem being solved. With respect to clustering, the weight of an edge may be a function of the spatial distance measured between two adjacent data points. In this way, a natural association with graph cutting and Bayesian estimation exists in that the edge weights may be thought of as prior probabilities that encode a priori knowledge about the physics of the system. As will be demonstrated below, this allows for an intuitive picture for the formulation of regularized inverse analysis problems and a computationally efficient framework for identifying optimal solutions.

The goal of this paper is to explore and demonstrate the applicability of the graph-cutting technique with respect to characterization of some inverse problems in materials science. Specific examples include image segmentation, atomic cluster identification, constituent phase segmentation, and parent grain identification from transformation microstructure (i.e. parent austenitic identification from the transformed martensite structure).

Methodology and Implementation

Regularization and Bayesian Estimation

Most readers will be familiar with the concept of regularization, a formal process for introducing additional information in order to solve ill-posed inverse problems. If we consider the standard linear problem for a known model matrix, $\mathbf{A}$, and vector of observations, $\mathbf{b}$, we wish to find $\mathbf{x}$ such that $\mathbf{Ax} = \mathbf{b}$. Ordinary least squares regression solves the problem by minimization of the sum of squared residuals as $\min_x||\mathbf{Ax}\text{-}\mathbf{b}||_2$. However, most imaging problems are underdetermined, meaning there are numerous possible solutions to the least squares problem. Regularization adds additional soft constraints in order to ensure selection of the "most desirable" solution (in some sense). Examples of regularization include Tikhanov regularization (Neubauer, 1989), which finds the solution with the smallest Euclidean norm; the least absolute shrinkage and selection operator (LASSO) (Tibshirani, 1996), which favors a sparse solution; and total variation (TV) (Rodríguez, 2013), which favors a smooth solution. The regularized problem is typically formulated as:

$$\min_x (||\mathbf{Ax} - \mathbf{b}||_2 + \lambda||f(\mathbf{x})||_p) \qquad (1)$$

Here, $||\mathbf{Ax}\text{-}\mathbf{b}||_2$ is the data fidelity term and ensures that the solution is consistent with the measured data and $f(\mathbf{x})$ is the regularization term ensuring the constraints.

Regularization can also be interpreted probabilistically or through a Bayesian lens. In terms of Bayesian inference, we are concerned with the probability of $\mathbf{x}$ given our observation $\mathbf{b}$, or $P(\mathbf{x}|\mathbf{b})$. In other words, we want to estimate the posterior probability distribution of $\mathbf{x}$ given the data we have observed. Using Bayes theorem, we can write:

$$P(\mathbf{x}|\mathbf{b}) = \frac{P(\mathbf{b}|\mathbf{x})P(\mathbf{x})}{P(\mathbf{b})} \qquad (2)$$

where $P(\mathbf{x}|\mathbf{b})$ is the posterior probability, $P(\mathbf{x})$ is the prior probability which encodes our belief about what $\mathbf{x}$ should be *before* observation and $P(\mathbf{b})$ is referred to as the evidence and gives the probability of obtaining the observation $\mathbf{b}$. Note that the prior probability is philosophically similar to the regularization, in the sense that it encodes what we believe the solution should "look" like. However, there is a subtle difference with equation (1): We are searching for the values of $\mathbf{x}$ that minimize our total cost whereas in the Bayesian sense we are looking for the maximizer of the posterior given our observations. Therefore, $p(\mathbf{b}|\mathbf{x})$ can be considered the Bayesian fidelity term which assures consistency between the added regularization, the observable data, and the obtained solution. In terms of an optimization, this refers to the maximum *a posteriori* probability, or MAP estimate, shown below:

$$\hat{\mathbf{x}}_{\text{MAP}} = \max_x P(\mathbf{x}|\mathbf{b})$$
$$= \max_x \left(\frac{P(\mathbf{b}|\mathbf{x})P(\mathbf{x})}{P(\mathbf{b})} \right) \qquad (3)$$
$$= \max_x (P(\mathbf{b}|\mathbf{x})P(\mathbf{x}))$$

Note that the evidence can be ignored since it is a constant with respect to the maximization. Many common regularization formulations have an exact equivalent MAP formulation, meaning the optimizations defined by equations (1) and (3) have the same solution. For example, Tikhanov regularization is equivalent to assuming a zero-mean Gaussian prior on $\mathbf{x}$, with λ (equation (1)) being expressed as a function of the variance (Johansen, 1997). Similar equivalences can be derived for LASSO and TV. For this work, we will favor a Bayesian interpretation as it aids in formulating the regularization problem as a graph, thus allowing for interpretation of the final graph cut solution.
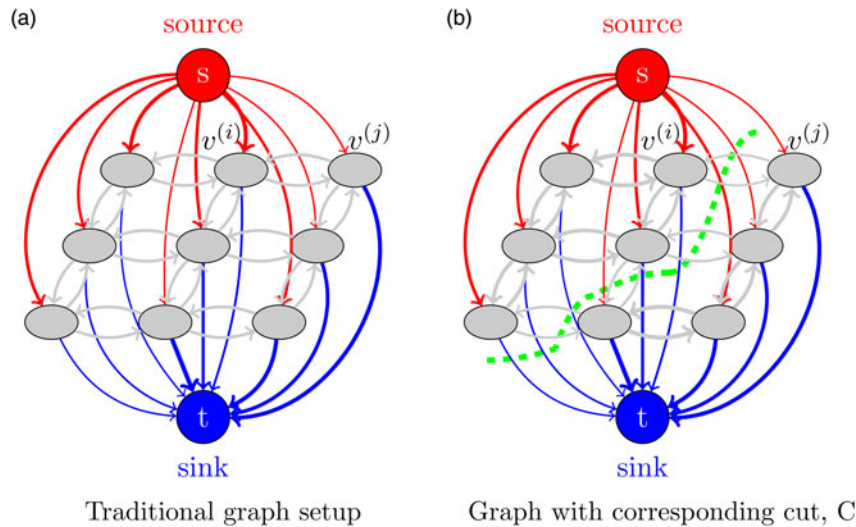
Fig. 1. Graph construction where *g* is separated by the terminal nodes, *s* and *t*. The *t-link* edges are colored in red and blue and the *n-link* edges are colored in gray, with the corresponding cut colored in green.

Graph Cut Notation

This section contains a brief description of some key definitions and notations used in this study. The interested reader can find a more complete description of graph theory, and graph cuts in particular, in reference (Boykov & Veksler, 2006). A graph, $\mathcal{G} = \mathcal{V}, \mathcal{E}$, consists of a set of *n* vertices or nodes, $\mathcal{V} = [v^{(1)}, v^{(2)}, \ldots, v^{(n)}]$, connected to each other by a set of *m* corresponding edges, $\mathcal{E} = [e^{(1)}, e^{(2)}, \ldots, e^{(m)}]$. The goal of the algorithm is to find an energy minimized cut, or maximum flow path, through the series of linked nodes. In terms of the latter, consider the edges connecting nodes as pipes with water flowing through them. The objective becomes redefined as a search for a series of interconnected pipes that will produce the maximum flow of water (max flow value) from the source to the sink. Pipes with a larger diameter will produce a higher flow rate, ergo severing the "thinner" pipes will result in a network of pipes that produce the maximum flow of water from the source to the sink. In general, edges may be either directed or undirected. A directed edge necessitates a direction of flow for a single edge, such that forward and reverse directions for two edges connecting the same set of nodes are not equal. An undirected edge refers to the opposite, where the forward and reverse edges connecting the same set of nodes are symmetrical. Associated with each edge, $e^{(k)}$, joining arbitrary nodes $v^{(i)}$ and $v^{(j)}$, is a weight, $w^{(k)}$. As $e^{(k)}$ is a directed edge, in general, $w(v^{(i)}, v^{(j)}) \neq w(v^{(j)}, v^{(i)})$. In other words, the flow between the nodes does not possess inversion symmetry.

The series of interconnected edges and nodes can be considered a *grid*, *g*, with the exclusion of two terminal nodes separating *g*, a *source*, *s*, and a *sink*, *t*. We can then define these subsets of non-terminal nodes, $\mathcal{P}$, and edges $\mathcal{N}(v^{(i)}, v^{(j)})$, as $(\mathcal{P} \in \mathcal{V} \wedge \mathcal{P} \neq s, t)$ and $(\mathcal{N}(v^{(i)}, v^{(j)}) \in \mathcal{E} \wedge \{v^{(i)}, v^{(j)}\} \subset \mathcal{N})$, the latter of which are referred to as *n-links* (Boykov & Veksler, 2006). Edges connecting $\mathcal{P}$ and *s* or *t* are denoted *t-links*, displayed below in Figure 1. Finally, weights can be classified into two sets by virtue of the edges they connect. In-plane weights $(w^{IP}(v^{(i)}, v^{(j)}) \wedge \{v^{(i)}, v^{(j)}\} \subset \mathcal{N})$ connect *n-links* and out-of-plane weights $(w^{OP}(v^{(i)}, v^{(j)}) \wedge \{v^{(i)}|v^{(j)}\} \equiv s|t)$ connect *t-links*, with each specific weight having a non-negative value associated with it.

Min-Cut/Max-Flow

A cut, $\mathcal{C}$, between *s* and *t* creates a partition of two distinct, mutually exclusive subsets, $\mathcal{S}$ and $\mathcal{T}$. The cost of the cut therefore becomes a function of these two partitions, $\boldsymbol{C} = \{\mathcal{S}, \mathcal{T}\}$, where it holds that $s \in \mathcal{S}$ and $t \in \mathcal{T}$. Mathematically, $\boldsymbol{C} = \{\mathcal{S}, \mathcal{T}\}$ can be interpreted as the summation of the weights of the aforementioned edges separating nodes within a continuous cut. Therefore, for any two arbitrary nodes, $v^{(i)}$ and $v^{(j)}$, separated by $\mathcal{C}$, it must follow that $v^{(i)} \in \mathcal{S}$ and $v^{(j)} \in \mathcal{T}$. The goal of the algorithm is to find an energetically favorable cut that minimizes the cost associated with dividing the graph into two subsets. While not proven here, it can be shown that, for the energy minimizing cut, the total flow through all severed edges is exactly equal to the maximum flow possible from *s* to *t* through $\mathcal{G}$. The Ford-Fulkerson theorem (Ford & Fulkerson, 1962) states that the saturation of a set of edges that divides a graph into subsets $\mathcal{S}$ and $\mathcal{T}$ can be achieved through a maximum flow from *s* to *t*, where the resultant cut is energetically minimized. Therefore, the energy minimized cut is equivalent to the maximum flow in the graph, and the two terms can be used interchangeably. A traditional graph setup can be seen in Figure 1, along with a partitioning cut traversing edges with arbitrarily low weights (depicted as thinner lines).

Graph Cutting Algorithm

In applications of graph cutting, several algorithms can be utilized to perform either the energy-minimized or max-flow cut. Greig et al. (1989) initially discovered that combinatorial optimization algorithms employing min-cut/max-flow techniques could be used for energy minimization in vision. Starting with labeling of an image, $\mathcal{L} = \{\mathcal{L}_{v^{(i)}} | v^{(i)} \in \mathcal{I}\}$, where $\mathcal{I}$ represents an image, the energy function can be set up as follows:

$$\mathcal{E}(\mathcal{L}) = \sum_{v^{(i)} \in \mathcal{I}} \mathcal{D}_{v^{(i)}}(\mathcal{L}_{v^{(i)}}) + \sum_{\{v^{(i)}, v^{(j)}\} \in \mathcal{N}} \mathcal{U}_{\{v^{(i)}, v^{(j)}\}}(\mathcal{L}_{v^{(i)}}, \mathcal{L}_{v^{(j)}}) \quad (4)$$

where $\mathcal{D}_{v^{(i)}}$ is a data penalty function and $\mathcal{U}_{\{v^{(i)}, v^{(j)}\}}$ is an interaction potential. Data penalties are typically incurred from observed
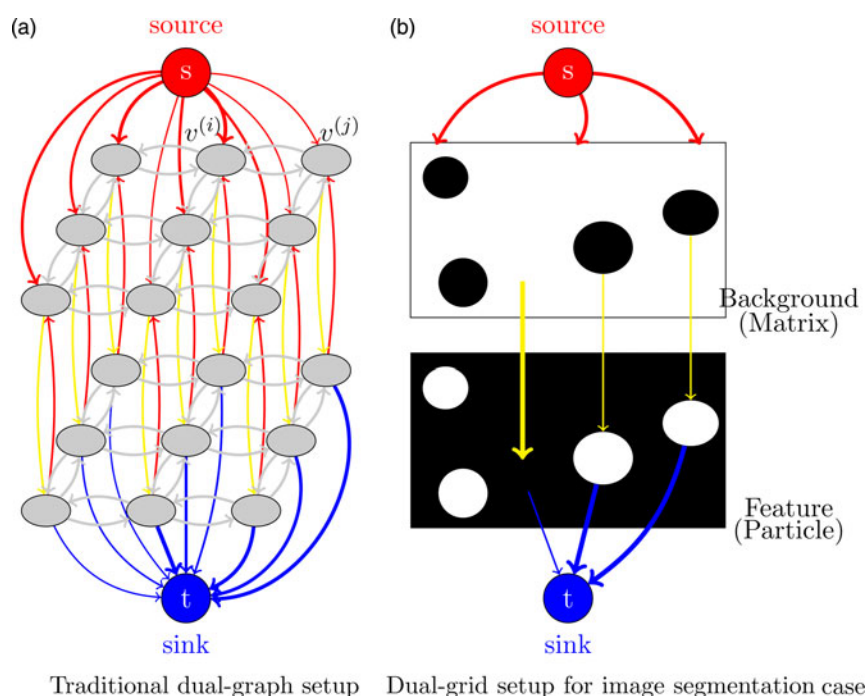
Fig. 2. The graph setup utilized to solve the problems mentioned in this paper along with a specified, arbitrary case involving image segmentation.

intensities and pre-specified likelihood functions on fixed, labeled pixels. The interaction potential penalizes discontinuities between neighboring pixels, thereby encouraging spatial consistency. This technique was limited due to the requisite binary nature of the problem setup and consequently remained stagnant for years. However, it gained momentum when min-cut/max-flow algorithms were introduced that could solve non-binary problems.

As such, three main groups of graph-cutting algorithms exist: Goldberg-Tarjan (Goldberg & Tarjan, 1988) "push-relabel" methods, Ford-Fulkerson (Ford & Fulkerson, 1962) "augmenting paths" implementation, and the newer "search tree" method (Boykov & Kolmogorov, 2004). The "maxflow" function within MATLAB (R2016a, Mathworks, Inc., Natick, MA USA) utilizing the Boykov–Kolmogorov "search tree" method is implemented in order to solve each of the subsequent problems described within this paper. For more detailed information on the aforementioned algorithms, refer to the following references (Cook et al., 1998; Boykov & Veksler, 2006).

Image Segmentation

Image segmentation is the process of partitioning an image into sets of related pixels in order to classify regions of the image or identify features in an image. In materials science, this is often applied to noisy images, where the goal is to identify and measure morphological attributes of microstructural features, propagate 3D structures from a series of 2D images, medical imaging, etc (Heimann & Meinzer, 2009; Faessel & Jeulin, 2010; Payton et al., 2010; Payton & Nolze, 2013; Waggoner et al., 2013). Accurate identification of features and separation from the background is critical for subsequent analysis of volume fraction, size, and spatial distributions of second phase particles, which typically have a large impact on properties and whose morphological distributions are strongly correlated to processing. Conventional image processing operations (simple

thresholding, opening, closing, dilation, erosion, etc.) are often found to be inadequate or require significant user intervention due to inhomogeneities in contrast and noise. Segmentation, specifically for materials imaging, has recently become reinvigorated with development of both machine learning approaches and new toolsets for stringing together new recipes of conventional image processing algorithms (Comer & Delp, 1994; Artan, 2011; Sosa et al., 2014; Campbell et al., 2018). The most prominent new image segmentation algorithm may be EM/MPM (Expectation-Maximization/ Maximization of the Posterior Marginals) (Comer & Delp, 1994, 2000; Simmons et al., 2009; Chuang & Comer, 2010). This approach is a stochastic algorithm which combines parameter estimation using the EM (Zhang et al., 1994) algorithm combined with a Markov random field (MRF) estimate for segmentation. The values for the marginal conditional probability mass functions are approximated in terms of the pixel label field through the use of the MPM (Marroquin et al., 1987) algorithm.

Graph Definition for Segmentation and Clustering

The general problem of image segmentation can be abstracted into the classification of all pixels in an image into two sets: those which belong to a feature of interest and a background consisting of all other pixels. As a specific instance, consider the identification of γ' particles from a background of the γ matrix in Ni and Co superalloys (El-Bagoury & Mohsen, 2011; Ramírez et al., 2016). For the segmentation problem, we introduce a different graph structure which contains two connected grids, denoted as g_1 and g_2, which correspond to the background and features of interest. This graph structure is shown schematically in Figure 2a.

The in-plane or intra-grid weights for g_1 and g_2 are identical for both grids and correspond to the probability that connected pixels come from the same set (either background or pixel), therefore existing as a measure of similarity between the pixels. Edges
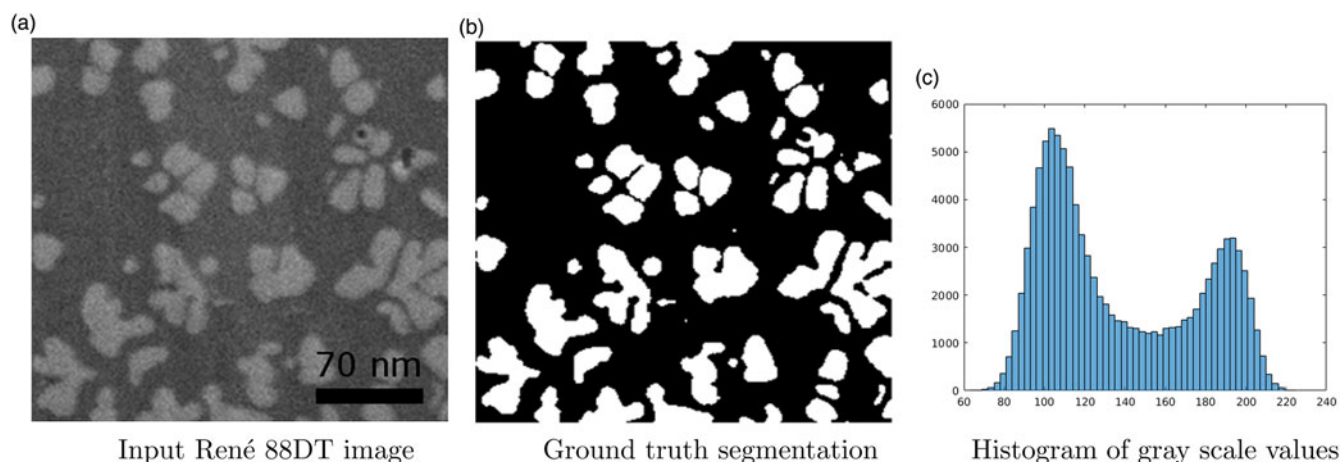
(a) Input René 88DT image (b) Ground truth segmentation (c) Histogram of gray scale values

Fig. 3. The graph schematic utilized to solve the problems mentioned in this paper along with a specified, arbitrary case involving image segmentation.

between pixels that are similar in intensity have higher weights than those that have significantly different intensities. This corresponds to the Bayesian *prior*, or interaction potential, between the pixels, $\mathcal{U}$ in equation (4). This leads to high penalties for cutting through edges that connect two similarly valued nodes and low penalties for placing an interface between pixels that differ strongly in intensity. The end result is continuous cuts that cluster like-nodes into the same family (background or feature).

The out-of-plane weights, associated with a subset of inter-grid edges, correspond to the data fidelity term $\mathcal{D}$ in equation (4) and are related to the probability that given pixels belongs to either the background or the feature of interest based on the intensity. The first set of out-of-plane weights, connecting each node in g_1 to the corresponding node in g_2, represents the likelihood that each pixel came from the background. A second set of out-of-plane weights, from each node in $g_2 \rightarrow t$, corresponds to the likelihood that the individual pixels belong to a feature of interest. In this way, the dual-grid system permits the effective separation of the system into background and features. This is schematically shown in Figure 2b, where red edges denote uncuttable weights from $s \rightarrow g_1$ and $g_2 \rightarrow g_1$, and the cuttable weights are represented with the following colors: gray edges indicate intra-grid weights, yellow edges stand for inter-grid weights connecting $g_1 \rightarrow g_2$, and the blue edges signify the second set of out-of-plane weights connecting $g_2 \rightarrow t$.

Additional inter-grid edges need to be introduced to complete the graph structure and prevent pixels from being assigned to either both the background and feature or neither set. It can be seen that all edges in the direction from $t \rightarrow s$ are also not cuttable. This structure ensures that, in order to separate s from t with a continuous cut, that (*i*) one and only one of the out-of-plane edges in the nodes in g_1 and g_2 associated with each pixel are cut and (*ii*) the corresponding in-plane edges related to the appropriate interface penalty are added when the class assignment changes between pixels. While adding some abstraction to the graph structure, this prohibits the cut from looping around a pixel and cutting both sets of out-of-plane-edges or cutting in-plane edges without a change of classification, ensuring topological consistency of the final cut.

Segmentation Examples

In order to demonstrate the efficacy of the graph-cutting algorithm for image segmentation, segmentations of the γ' phase in

$\gamma - \gamma'$ Ni superalloys (René 88DT (MacSleyne et al., 2009) and René 104 (Payton et al., 2010, 2011)) from backscattered electron (BSE) images were performed. Direct comparisons were prepared using three separate techniques–the well-established Otsu threshold method (Otsu, 1979), the modern EM/MPM algorithm (Comer & Delp, 2000), and the present graph cutting procedure.

Figure 3 shows the original grayscale BSE image, a histogram of the pixel intensities, and a ground truth segmentation for the René 88DT image (Uchic & MacSleyne, 2006). As can be seen from the histogram (Fig. 3c), the intensity distribution from both phases overlap, resulting in an ambiguity of class assignment for a range of intensities. The ground truth image, found in Figure 3b, was obtained from BlueQuartz Software (Uchic & MacSleyne, 2006) and was constructed by first applying a threshold to obtain a first estimate of the ground truth segmentation. Then Photoshop™ was utilized to further manually classify individual pixels as either part of a particle or the matrix (Uchic & MacSleyne, 2006). The Otsu method chooses a single threshold value based on a minimization of the intra-class variances of the feature and background (Otsu, 1979). For this image, a grayscale threshold value of 0.322 was used. For the EM/MPM segmentations, the exchange energy and number of iterations (loops) were optimized to find the best segmentation. Optimal segmentations were found with an exchange energy of 1.5 with five total segmentation loops.

The graph for the segmentation problem was defined as follows. Each individual pixel within the input micrograph was labeled as $v^{(i)} \in g_k$, and the respective intensity value for each node was used to construct the *prior*. An adjacency array was constructed between each node and the set of four nearest neighbors. The in-plane weights between neighboring pixels were then computed as:

$$w^{IP}(v^{(i)}, v^{(j)}) = \lambda \left(\frac{1}{|I(v^{(i)}) - I(v^{(j)})|} \right) + \beta \qquad (5)$$

where $I(v^{(i)})$ is the intensity of the pixel associated with node $v^{(i)}$ and λ is a meta-parameter which controls the degree of regularization or the balance between fidelity and interaction energy. Since it holds that if two neighbored pixels have the similar grayscale values, it is more likely that they belong to the same class, inverting these values effectively penalizes the graph-cutting algorithm for
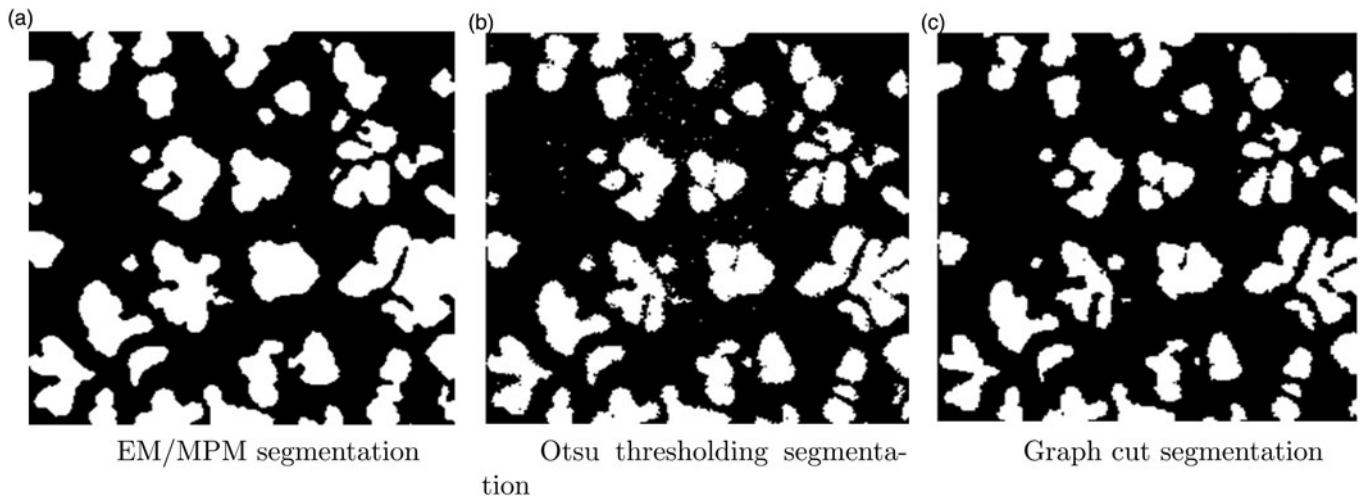
Fig. 4. The graph setup utilized to solve the problems mentioned in this paper along with a specified, arbitrary case involving image segmentation.

making a cut between these nodes. This increases the probability that these nodes would be clustered together. In contrast, cutting between neighboring pixels with greatly disparate intensities would be highly favored. The β parameter adds a uniform penalty for making any in-plane cut, and can be thought of as being analogous to the interfacial energy between the phases. A high value of β is useful in highly noisy images or heavily overlapped histograms and acts to enforce that the segmented features are compact and connected. For this image, $\lambda = 2.55$ and $\beta = 10.5$ values were used. In principle, the penalty associated with regularization of interaction energy can be any arbitrary function. Other choices could include second-nearest or higher-order neighbors (increase the number of edges) or other modifications to the penalty, including adding an ignoring intensity mismatch for obviously bad pixels such as from salt-and-pepper noise (identical intensity values of 0 or 1 which can occur during analog to digital conversion) (Torre & Poggio, 1986; Poggio et al., 1988; Bovik, 2000; Chan et al., 2005).

The out-of-plane weights were established by modeling the intensity distributions for the background and feature pixels as independent Gaussian distributions with means $[\mu_\gamma, \mu_{\gamma'}]$ and standard deviations $[\sigma_\gamma, gma_{\gamma'}]$ for the background γ and feature γ' phases, respectively. The first set of out-of-plane weights, which connect $g_1 \rightarrow g_2$, are proportional to the probability that each pixel is a member of the background given its intensity, and was calculated using the following equation:

$$w^{g_1 \rightarrow g_2}(v^{(i)}) = f\left(I(v^{(i)}) | \mu_\gamma, \sigma_\gamma\right)$$
$$= \alpha_\gamma \left(\frac{1}{\sigma_\gamma \sqrt{2\pi}} \exp \left(\frac{-(I(v^{(i)}) - \mu_\gamma)^2}{2\sigma_\gamma^2} \right) + \omega_\gamma \right) \quad (6)$$

Here, $v^{(i)}$ is the node in g_1 associated with pixel i, α is a scaling parameter analogous to λ in equation (5) and ω is a user-defined penalty term similar to β in equation (5). For the René 88DT image, values of 2.75 and 4.45 were used for α_γ and $\alpha_{\gamma'}$ and 2.75 and 8.55 for ω_γ and $\omega_{\gamma'}$, respectively. The second set of out-of-plane weights from $g_2 \rightarrow t$ are defined in a completely analogous manner with $\mu_{\gamma'}$ and $\sigma_{\gamma'}$ replacing the mean and standard deviation for γ.

After designating both sets of weights, the graph cut algorithm is exercised to find the energy minimized cut that segments all of the particles from the matrix. The results for the graph cut segmentation are given below in Figure 4, along with the results for the Otsu thresholding and EM/MPM segmentation on the same image.

Images of superalloy microstructures often contain particles that are more difficult to distinguish from the matrix using automated image processing than those shown in Figure 3a. The gray scale values show a smooth blend between each other, limiting the range of the bimodal RGB/gray scale distribution and effectively minimizing distinguishing factors. Therefore, a second segmentation on a truncated section of the nickel-based superalloy René 104 characterized by Payton et al. (2010, 2011) with less contrast between particles and matrix was performed for further validation of the graph cutting algorithm relative to other available approaches. The overlap of grayscale values between particle and matrix is displayed in the histogram in Figure 5c. The parameterization for all three segmentation methods for the René 104 image are as follows: the Otsu thresholding value was determined to be 0.498, the energy exchange parameter for EM/MPM (β in reference Duval et al. (2014)) was found to be 1.7, with 5 iteration/segmentation loops performed, and the graph-cutting procedure had values of $\lambda = 6.0$, $\beta = 0$, $\alpha_\gamma = 1.0$, $\omega_\gamma = 1e^{-2}$, $\alpha_{\gamma'} = 1.0$ and $\omega_{ma'} = 1.7$, respectively. The ground truth image was obtained through meticulous use of MS Paint. The input image was magnified to the point where discrete pixels were visible and pixels were manually marched across from border to border, subsequently coloring particles white and the surrounding γ matrix black. A threshold was then applied to rid the image of any non-binary pixels and reclassify them accordingly, as either particle or matrix, to rid the image of any residual noise. The segmentations for all three methods are shown in Figure 5.

As the results in Figures 4 and 5 show, the graph-cutting algorithm does a comparably good job of segmenting the image. The particle features mimic the geometry found within the ground truth sample, although all techniques have trouble identifying separate but spatially close particles that are clustered into groups. In order to determine how effective each method was in performing the segmentation, through consideration of the ground truth dataset as the signal, the signal-to-noise ratios (SNR) for all three techniques can be computed through the following equation:

$$SNR = 20^* \log \frac{||S_0||_F}{||S_0 - S_n||_F} \quad (7)$$
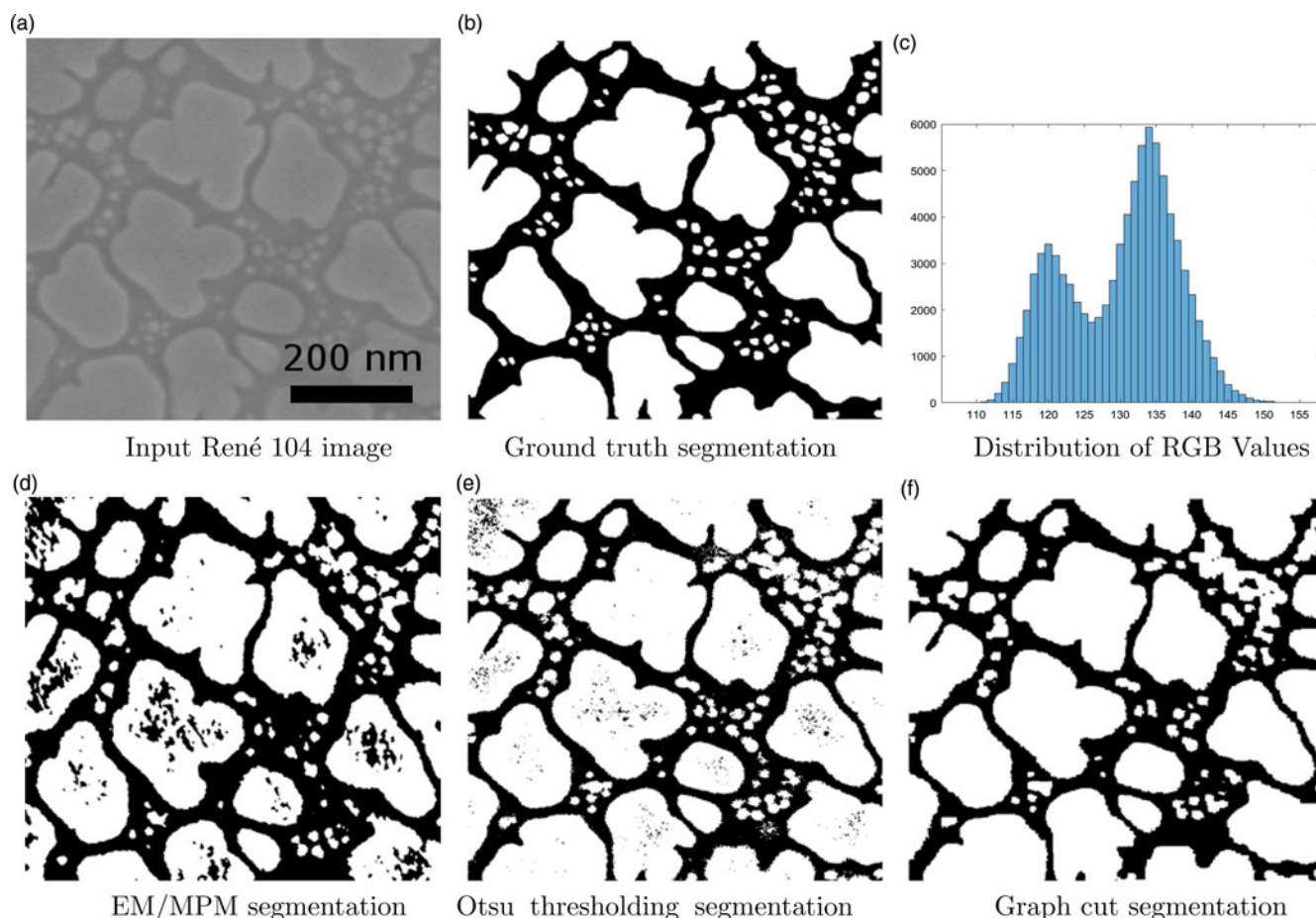
Fig. 5. Input image, ground truth segmentation, and pixel-intensity histogram for the René 88DT dataset.

Table 1. The SNR Values for the EM/MPM, Otsu Threshold, and Graph Cutting Segmentations.

	EM/MPM	Otsu Threshold	Graph Cut
René 88DT	17.74	24.12	23.14
René 104	5.58	17.02	17.97

where S_0 represents the clean image (ground truth), S_n is the noisy image (segmented image), and the notation $||...||_F$ represents the Frobenius norm. The SNR values for each segmentation are given below in Table 1.

The SNR for the graph cut segmentation is found to be better than the segmentation performed using EM/MPM for both images, especially considering the case of the René 104 image where the greater overlap is found in the contrast histogram. In terms of the Otsu thresholding method, the SNR value is higher than the graph-cutting value for the René 88DT image. This is most likely due to the fact that a large contrast between matrix and particle grayscale values exists, which allows for effective segmentation using the simplest possible algorithms.

In comparison to Otsu and EM/MPM, the graph-cutting method does a better job of capturing the extent of larger particles without requiring a hole filling step, especially when a grayscale gradient exists within the particle (as in the case of the René 104 particles, *cf.* Figure 5). However, both Otsu and EM/MPM

are better at distinguishing the smaller tertiary γ' particles from the matrix. For this population of particles, the present graph cut algorithm tends to merge more clusters of closely spaced particles. Overall, the graph cut approach results in a cleaner image with respect to the more difficult to segment René 104 dataset, with EM/MPM producing a significantly lower SNR than the other methods for both datasets.

Microstructure Phase Segmentation and Identification

Identification and Segmentation of Bainite and Martensite

The ability to quantitatively characterize the volume fractions and spatial arrangements of microstructural constituents remains a challenge in hyperspectral or multi-modal datasets, in which the data collected comes from multiple acquisition modes or there is a spectrum of values for each spatial coordinate. This characterization problem is particularly complex in materials where the microstructural features of interest are characteristic arrangements of phases, as is often the case with advanced steels. This includes transformation induced plasticity (TRIP) steels, dual-phase (DP) steels, and complex phase (CP) steels, where there can be significant overlap between the signals for austenite, ferrite, bainite and/or martensite (Kang et al., 2011). In terms of the latter two, it becomes exceedingly difficult to segment these microstructure constituents due to their shared plate-like morphologies. Although the bainite transformation takes place at a

temperature above the martensite transformation temperature, commercially relevant heat treatment processes can result in a mixture of the two constituents which can have important effects on the mechanical properties of the post-processed material (Davies, 1978). Therefore, as a second case study, we have applied the graph-cutting technique to microstructure constituent segmentation in steels through use of EBSD-measured kernel average misorientation (KAM) values, which are the average misorientation angles between a discrete point and a kernel of its neighboring points.

Experimentally, several techniques have been used in the characterization of microstructure constituents. Typically, the surface preparation of the sample drives the identification of different microstructures of steels. For example, certain etchants can magnify the contrast between phases and/or microstructural constituents by distinguishing them as colored regions (LaPera, 1978; Girault et al., 1998). However, these color-etching methods are difficult to reproduce and the color ranges of microstructure constituents (most notably martensite and bainite) overlap. The color etching is also limited by the spatial resolution of optical microscopy. Significant overlap also exists between the gray levels of constituents in SEM imaging (Tan, 2017; Tan et al., 2018).

Tackling the issue through computational methods seems to be even more difficult as the significant overlap between the observable bainite and martensite characteristics makes it difficult to distinguish between the constituents. Wu et al. (2005) investigated the variation in EBSD pattern image quality (IQ) with microstructure constituent and showed that, while significant overlap in the signals existed, the differences in IQ can provide useful information for identifying and locating microstructure constituents in multiphase steels. IQ is a data that describes the level of contrast within the collected backscatter diffraction pattern but it can also correlate to the local elastic strain, thermodynamic phases, proximity to interfaces and interface properties, and the defect state of the microstructure (Hutchinson et al., 1998; Keller et al., 2004; Petrov et al., 2007; Wright et al., 2011; Tolba & Raafat, 2015; Shinozaki et al., 2016). Zaefferer et al. (2008) utilized KAM values in order to separate a mixture of ferrite, bainite, and austenite in an Al-TRIP steel, but for practical application of the technique it is found that reproducibility is limited by a subjective identification of the relevant features in the KAM histogram, which for many alloys differ significantly from the KAM histogram of the material analyzed in their work.

Tan (2017) and Tan et al. (2018) used KAM values to estimate the volume fractions for each constituent using a KAM deconvolution distribution mixture model. Although this method produces relatively accurate volume fractions for each constituent, it lacks the ability to resolve the locality of constituents and phases. Therefore, based on the observations of Zaefferer et al., Tan et al., Wu et al., and others, utilizing the correlations between pattern quality, KAM, and microstructure constituent seems to bode well for application of a graph cut algorithm through consideration of distributions of values for the individual phases in multimodal or hyperspectral datasets such as those obtained by EBSD.

A key benefit of the graph cut approach is the flexibility in how the data fidelity and interaction potential are formulated. For this example, we will use the KAM angles to define the data fidelity component and EBSD Image Quality (IQ) values for the interaction potential. In formulating the interaction potential based on IQ, the underlying assumption is if neighboring data points have similar IQ values, there is a high probability of them belonging to the same phase.

In order to test the graph-cutting algorithm in terms of microstructural constituent segmentation on hyperspectral data, an EBSD dataset from AISI 5160 steel, provided by Tan (2017) and Tan et al. (2018), was used to create a segmentation case study. The steel samples were processed through austenization and subsequent heat treatment and quenching to acquire specimens comprised nearly completely of a single constituent (martensite, bainite, and ferrite) at the same nominal chemical composition. Corresponding distributions for the KAM values of these specimens were computed using TSL OIM™ Analysis 7 applied to third nearest neighbors, with a maximum KAM value of 5° applied to training EBSD datasets. Any values above this threshold were considered either noise or grain boundary pixels and were appropriately flagged.

Analogous to the segmentation of BSE images, the out-of-plane weights were assigned by considering the probability of phase assignment. The distribution of KAM angles for each phase was again assumed to be independent of the other phases and Gaussian. Let P = {martensite, bainite, ferrite, …} be the set of phases of interest, indexed by ρ. For phase ρ, the discrete probability density of the KAM angle, Θ, is given by $P_\rho(\Theta)$. The mean and standard deviation of KAM angles Θ for each phase can then be given by:

$$\mu_\rho = E\big(\Theta_\rho(j)\big) = \sum_\theta \theta_\rho * P_\rho(\Theta = \theta)$$
$$\sigma_\rho = \sqrt{\sum_\theta (\theta_\rho - \mu_\rho)^2 * P_\rho(\Theta = \theta)} \tag{8}$$

where $E(\cdot)$ is the expectation operator. These values, calculated from the single component datasets, were then used for segmentation of EBSD datasets containing a mixture of all three constituent microstructures.

As in the segmentation of BSE images, the distribution of the out-of-plane weights for the segmentation case study is given by:

$$w^{g_1 \to g_2}(v^{(i)}) = f\big(\Theta(v^i)|\mu_\rho, \sigma_\rho\big) \tag{9}$$

which is identical to equation (6), with the KAM angle distribution for phase ρ replacing the pixel intensity distribution and the α parameter set to unity. Again, the out-of-plane weights for the other phases are formulated in a manner analogous to equation (6).

As described above, the interaction penalty or regularization is formulated as a function of EBSD Image Quality (IQ). Assuming that similar IQ values would indicate two adjacent points came from the same constituent, the in-plane weights for adjacent nodes were computed through a normalized difference of these values:

$$w^{IP}\big(v^{(i)}, v^{(j)}\big) = \left|\left| \lambda \sqrt{\frac{1}{IQ(v^{(i)}) - IQ(v^{(j)})}} \right|\right| + \beta \tag{10}$$

where the regularization parameters were set as $\lambda = 2^2$ and $\beta = 0$. The out-of-plane edges associated with EBSD points containing KAM values outside the range $\Theta > 5°$ were assigned equal but numerically small ($w \approx 0$) for each of the potential constituents. This ensures that the interaction penalty or regularization term dominated, thereby heavily favoring each pixel's local neighborhood in phase or constituent assignment.
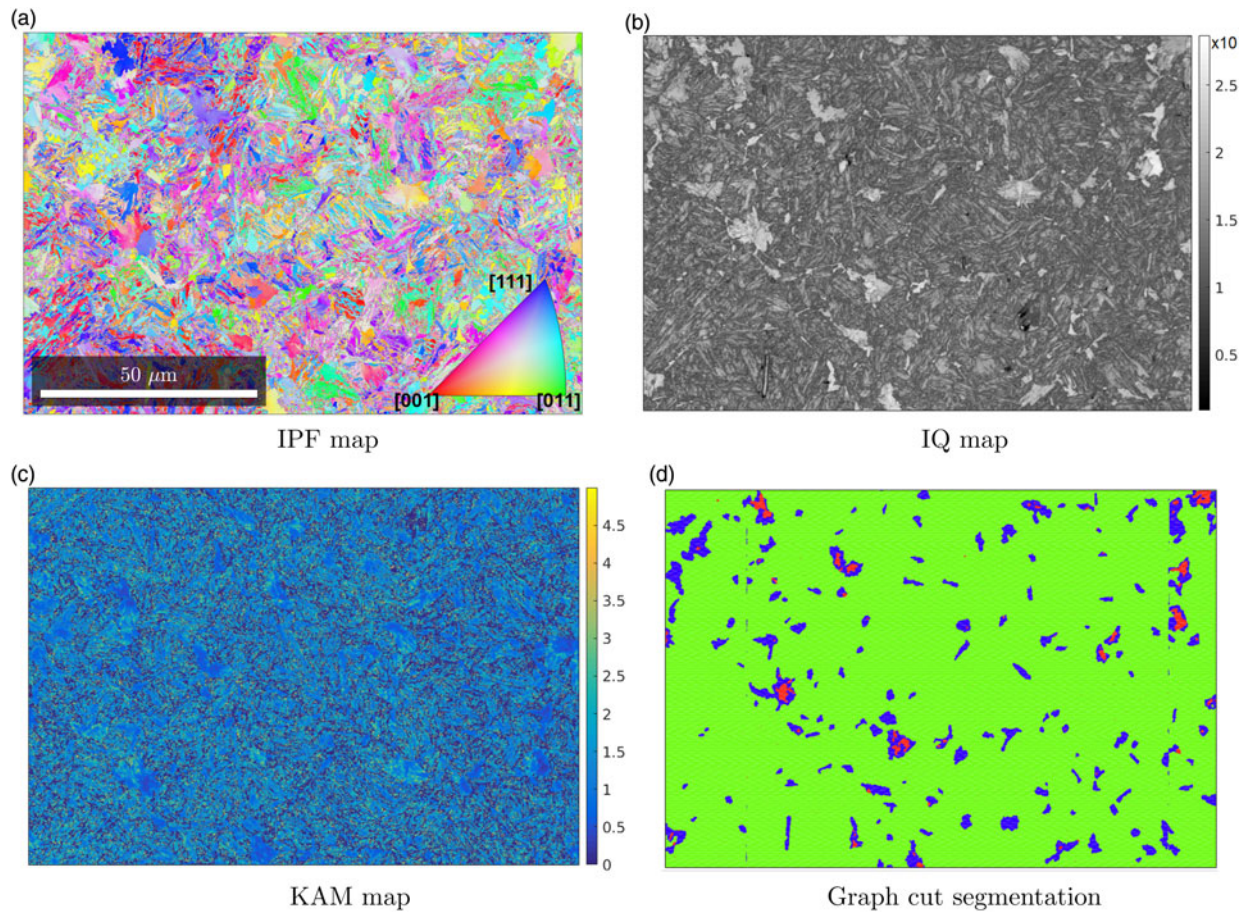
Fig. 6. Series of segmented images using various segmentation techniques for the René 88DT dataset.

As there are three microstructure constituents of interest in this example, the graph structure for the complete problem should contain three grids. However, since bainite and martensite are so similar with respect to their KAM distributions, the problem was solved in two stages. The first cut involved segmenting ferrite from the background of martensite and bainite, using a two grid graph structure. For the next cut, the identified ferrite was removed from the EBSD dataset, and a second cut was made segmenting the martensite from a background of bainite. The cuts can be seen in Figure 6, along with the corresponding IQ and KAM maps. The graph cut segmentation generally locates the correct bainitic regions within the martensite matrix and finds plausible locations for proeutectoid ferrite adjacent to the bainite. The volume fractions predicted by the graph cut are in good agreement with those predicted by the KAM distribution deconvolution method of Tan (2017) and Tan et al. (2018), as shown in Table 2. Respective volume fractions for ferrite, bainite, and martensite using the graph-cutting technique and KAM distribution deconvolution (Tan et al., 2018) method.

Prior Austenite Grain Identification

The motivating application for the development of the graph-cutting technique was the identification of parent grains given EBSD datasets of a transformation microstructure (e.g. identification of prior β grains from α Ti microstructures or identification of austenite grains from observations of martensite). In terms of the austenite $\rightarrow$ martensite transformation $(\gamma \rightarrow \alpha')$, the athermal

Table 2. Respective Volume Fractions for Ferrite, Bainite, and Martensite Using the Graph Cutting Technique and KAM Distribution Deconvolution Tan et al. (2018) Method.

	$v_f(fer)$ (%)	$v_f(bain)$ (%)	$v_f(mart)$ (%)
KAM Distribution Deconvolution (Tan 2017; Tan et al. 2018)	1	6	93
Graph Cut	1.0	6.5	92.5

transformation results in a series of martensite laths exhibiting 24 crystallographic variants (Morito et al., 2003; Kitahara et al., 2006). Although the martensite microstructure controls the effective mechanical properties of the material, localization, and failure can be heavily influenced by the prior austenite microstructure, including increasing prior austenite grain (PAG) diameters affecting ductile to brittle fracture occurrence (Kimura et al., 1987; Yardley et al., 2012), the classification of creep and cavitation sites (Hong & Yu, 1989; Yardley et al., 2015), and temper embrittlement due to impurity segregation at prior austenite grain boundaries (Banerji et al., 1978; Horn & Ritchie, 1978). For many alloy compositions, the transformation goes to completion such that inferences on the prior austenite microstructure can only be made from observations on the transformed martensitic microstructure. Determining the prior austenite orientation is complicated by uncertainty in the

EBSD orientation indexing, the prevalence of annealing twins in the austenite, variation in the OR with composition, and heterogeneous plastic deformation due to accommodation of the martensitic shear (Wayman, 1975; Sandvik & Wayman, 1983; Kelly et al., 1990; Morito et al., 2003; Shibata et al., 2009; Gnäupel-Herold & Creuziger, 2011; Abbasi et al., 2012).

Several prior austenite reconstruction algorithms exist, typically employing similar flood-fill-like approaches in which the misorientations between potential prior-austenite orientations of neighboring pixels are analyzed and compared with a tolerance (Cayron, 2007; Bernier et al., 2014; Hata et al., 2017; Cluff et al., 2018). If the misorientation falls below the tolerance, the two martensitic points are considered to come from the same PAG and are grouped together. This continues between neighboring points until the tolerance cannot be reached, at which point a grain boundary is drawn between points and the process starts over at another node. For our procedure, we want to demonstrate, in a proof-of-concept manner, that it is feasible to use graph-cut segmentation to simultaneously identify all of the martensite points contained within a prior-austenite grain. This will serve as a basis for the development of a complete reconstruction algorithm but, for the purposes of this paper, serves as an additional case study for demonstrating the utility of the graph-cut method for a wide range of segmentation problems. The extension of single grain segmentation to a complete polycrystalline austenite reconstruction algorithm is beyond the scope of this paper and will be detailed in a subsequent paper. The EBSD dataset used for this example came from a 9 to 12%Cr tempered martensite ferritic steel, for which more information is available in reference (Yardley et al., 2012). While the orientation relationship (OR) is well-known to vary with composition (Greninger & Troiano, 1949; Payton et al., 2012; Brust et al., 2019), for the purposes of the example we will simply assume a Kurdjumov–Sachs (KS) orientation relationship (Kurdjumow & Sachs, 1930).

Consider an EBSD dataset of a completely martensitic structure, where the martensite orientation measurements can be labeled, $G_m = [g_m^{(1)}, g_m^{(2)}, \ldots, g_m^{(n)}]$ and correspond to graph vertices $\mathcal{V} = [v^{(1)}, v^{(2)}, \ldots, v^{(n)}]$. Note that this labeling, and the resultant graph structure is agnostic with respect to the EBSD sampling grid (either square or hexagonal). Following the pattern of the previous examples, the weights of the in-plane edges should relate the probability that the martensite orientations measured at two neighboring EBSD scan points are consistent with coming from the same PAG. In previous work, the authors described the set of possible martensite-to-martensite misorientations given a common parent (Brust et al., 2019). Payton et al. (2012) have characterized the degree of scatter, or variability in the OR observable from EBSD. From this information, a martensite–martensite misorientation distribution function (MODF) can be constructed and denoted $f(\Delta G_m)$. The MODF was constructed by convolving the admissible martensite–martensite misorientations with a de La Valee Poussin kernel function (Bachmann et al., 2010). The half-width of the kernel was taken as $1.7°$ to best match the variability observed by Payton et al. (2012). The misorientation between the two martensite orientations associated with the edge with end vertices $v^{(i)}$ and $v^{(j)}$ is denoted $\Delta g_m(v^{(i)}, v^{(j)})$, and the in-plane weights can then be calculated as:

$$w^{IP}(v^{(i)}, v^{(j)}) = \lambda \Delta(g_m(v^{(i)}, v^{(j)}) + \beta \quad (11)$$

The out-of-plane weights are related to the probability that the martensite orientations, G_m, were generated from a trial austenite orientation, g_a. If the austenite → martensite OR is denoted $\Delta g_{a \to m}$, then $f(g_m | g_a, \Delta g_{a \to m})$ denotes an ODF which gives this probability. The term $f(g_m | g_a, \Delta g_{a \to m})$ can be constructed by convolving the trial austenite orientation with a kernel with suitable half-width to create a unimodal ODF. The ODF can be transformed by all variants of the OR, $\Delta g_{a \to m}$, producing an ODF with 24 peaks, each corresponding to one martensite variant from the given parent. For this example, the weights $w^{g_2 \to t}(v^i)$ are simply:

$$w^{g_2 \to t}(v^i) = \lambda f(g_m | g_a, \Delta g_{a \to m}) + \beta \quad (12)$$

The weights $w^{g_1 \to g_2}$ relate to the probability that a data point is part of the background. In this case, the background refers to all martensite orientations that did not come from a parent grain with orientation g_a. This can be approximated by the uniform ODF which is unity for all orientations, giving us:

$$w^{g_1 \to g_2} = \lambda f_{\text{uniform}}(g) + \beta = \kappa \quad (13)$$

A portion of the transformed microstructure was analyzed to find a region of interest that did not include any twins. A small but sufficient section of this region was then extracted and each martensite orientation was transformed through the 24 crystallographic variants into austenite. A local austenite ODF was finally computed and a relative maximum g_a was chosen as the guess orientation to perform likelihood calculations on.

Figure 7a shows the input EBSD dataset, with orientations colored according to a standard cubic IPF key found in Figure 6. Figure 7b maps the likelihood $f(g_m | g_a, \Delta g_{a \to m})$ for the evaluated-trial austenite orientation. Lighter values indicate higher likelihoods and the darker points correspond to low likelihood positions. High likelihood values are concentrated within the boundary of the central PAG in the image, suggesting a reasonable austenite guess orientation was chosen, while a few scattered high likelihood points appear generally well separated within the plot. Figure 7c shows the result of the graph cut, colored again using a cubic IPF key such that the color of the segmented region corresponds to the guessed prior austenite orientation. The background of scattered colors is related to an array of randomly assorted austenite orientations at each individual point assuming a completely transformed microstructure. Since the chosen austenite orientation is highly favored within the central PAG but nowhere else, it is consistent that the likelihood values in Figure 7 corresponding to these random orientations are low (~ 0).

In order to assess the potential efficacy of our proposed method, a grain boundary misorientation tolerance method was applied through MTEX. (Bachmann et al., 2010) This method employs a similar misorientation-based methodology adopted by some austenite reconstruction codes. This was accomplished by computing the 16 theoretical martensitic misorientations corresponding to a single PAG for variants generated from the KS OR. The grain boundary misorientations from the input data were then calculated and a spatially resolved list was generated detailing each respective misorientation. The grain boundary misorientations were finally compared with the PAG-induced martensite misorientations with respect to a user-defined tolerance. Higher tolerances mean more grain boundary misorientations are accepted as having come from the same PAG and subsequently assigned an austenite orientation, whereas lower tolerance values create more stringent acceptance guidelines. Additionally,
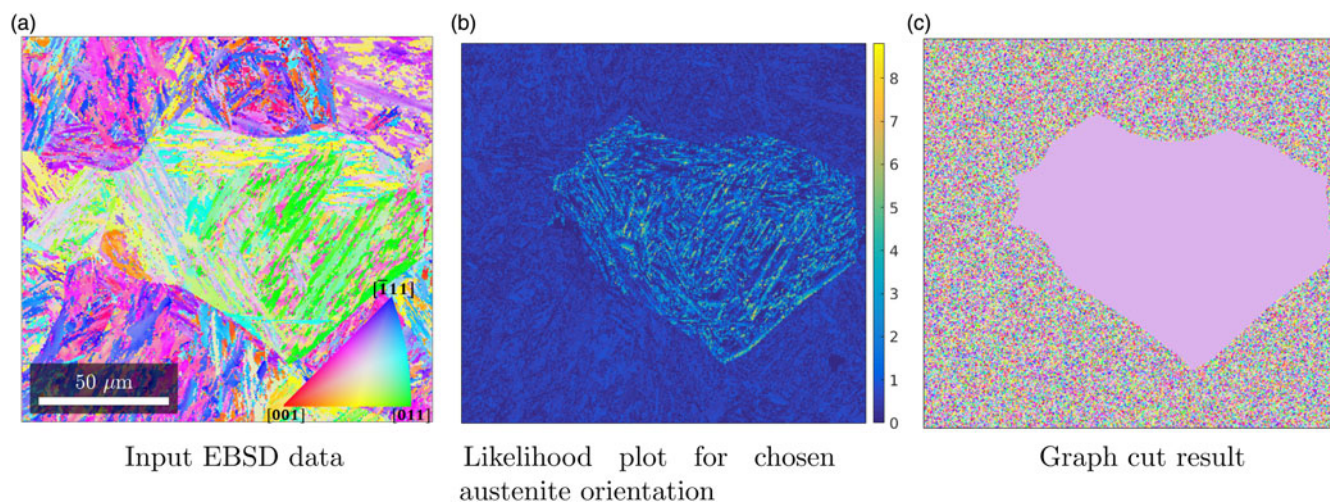
Fig. 7. Segmentations and input texture for René 104 nickel-based superalloy.

each austenite grain is colored by a unique grain ID to easily distinguish between reconstructed grains. The resultant full austenite reconstructions can be seen below in Figure 8 for several tolerances.

Atomic Clustering

Detailed analyses and descriptions of microstructures, including classification of precipitates and clustered atoms in solid solutions, can be achieved through the use of atom probe tomography (APT). Spatially correlated atoms within a solid solution can be used to identify clusters of atoms, which in turn serve as precursors to spinodal decomposition, precipitation, and chemical ordering (Felfer et al., 2015). Although several clustering techniques have been applied to APT data, including *k*-means clustering (MacQueen, the maximum separation method (Hyde & English, 2000), the core-linkage algorithm (Stephenson et al., 2007), Voronoi Partitioning (Felfer et al., 2015) and Gaussian mixture model Expectation Maximization Algorithm (Zelenty et al., 2017)), they often require extensive manual intervention and have difficulty in segmenting clusters within a dense background of uniformly distributed atoms. As a final example of applications of the graph-cut method we explore the potential for analysis of APT data by performing cluster identification and analysis for simulated 2D "APT-like" datasets. This final case study also demonstrates how the graph-cut approach can easily be extended to data that is not on a regular grid.

The setup for the identification of clustered atoms given synthetic ATP data was similar to the ones used for the aforementioned segmentation examples, including the one displayed in Figure 2b. The differences that arise between the clustering and segmentation examples are minimal in terms of implementation into our graph cutting algorithm and highlight the versatility of the technique in terms of grid construction. Mainly, instead of a square grid for image pixel intensities or hexagonal or square grid for phase and parent grain segmentation, the grid can be randomly assigned based on the coordinates of each individual atom with respect to an arbitrary reference frame. This allows for the spatial distance between neighboring atoms to be utilized to generate pertinent weights for each system based on the classification of atoms as coming from either a cluster (smaller distances

between neighboring atoms) or the background (larger distances between atoms). The dual-grid setup is shown schematically below in Figure 9 for an arbitrary system of atoms, represented as the black circles. Again, the $s \rightarrow g_1$ edges are uncuttable and displayed in red, and the yellow edges from $g_1 \rightarrow g_2$ indicate the probability that atoms came from the background. The blue edges then constitute the probability that atoms are situated within clusters. Finally, the gray intra-grid edges found between neighboring atoms have thicknesses proportional to spatial distances, where thicker edges are found between atoms that are spatially nearer to each other.

Each respective system was then established through the use of weights, and each atom comprising the entire system was considered a node $v^{(i)}$ within g_k. The versatility of node placement is most notable for this set up as the distances between adjacent nodes are entirely random, fluctuating both relative to the population of atoms within the system and how dense the population is that surrounds any given atom. The in-plane weights were computed through the calculation of discrete, multivariate probability distributions for each atom's specific coordinates, x, using the following equation:

$$w^{IP}(v^{(i)}, v^{(j)}) = f(X, x, \Sigma)$$
$$= \frac{1}{\sqrt{|\Sigma|(2\pi)^2}} \exp\left(-\frac{1}{2}(X - x)\Sigma^{-1}(X - x)'\right)$$

(14)

where x represents the entire distribution of atoms in a 2D Cartesian coordinate frame and Σ is the covariance matrix. Through consideration of each atom as an individual distribution, spatial correlations for each atom with respect to the rest could be quantified. This assisted in the identification of regions of dense populations, thereby allowing the algorithm to effectively group atoms within these regions as likely clustered atoms.

The out-of-plane weights were computed through utilization of the discrete multivariate probability distribution values. The population density composition of in-plane weights resulted in a bimodal distribution of values detailing the likelihood that an atom belongs to a cluster or the background. This allowed for the assignment of respective μ and σ values since clustered
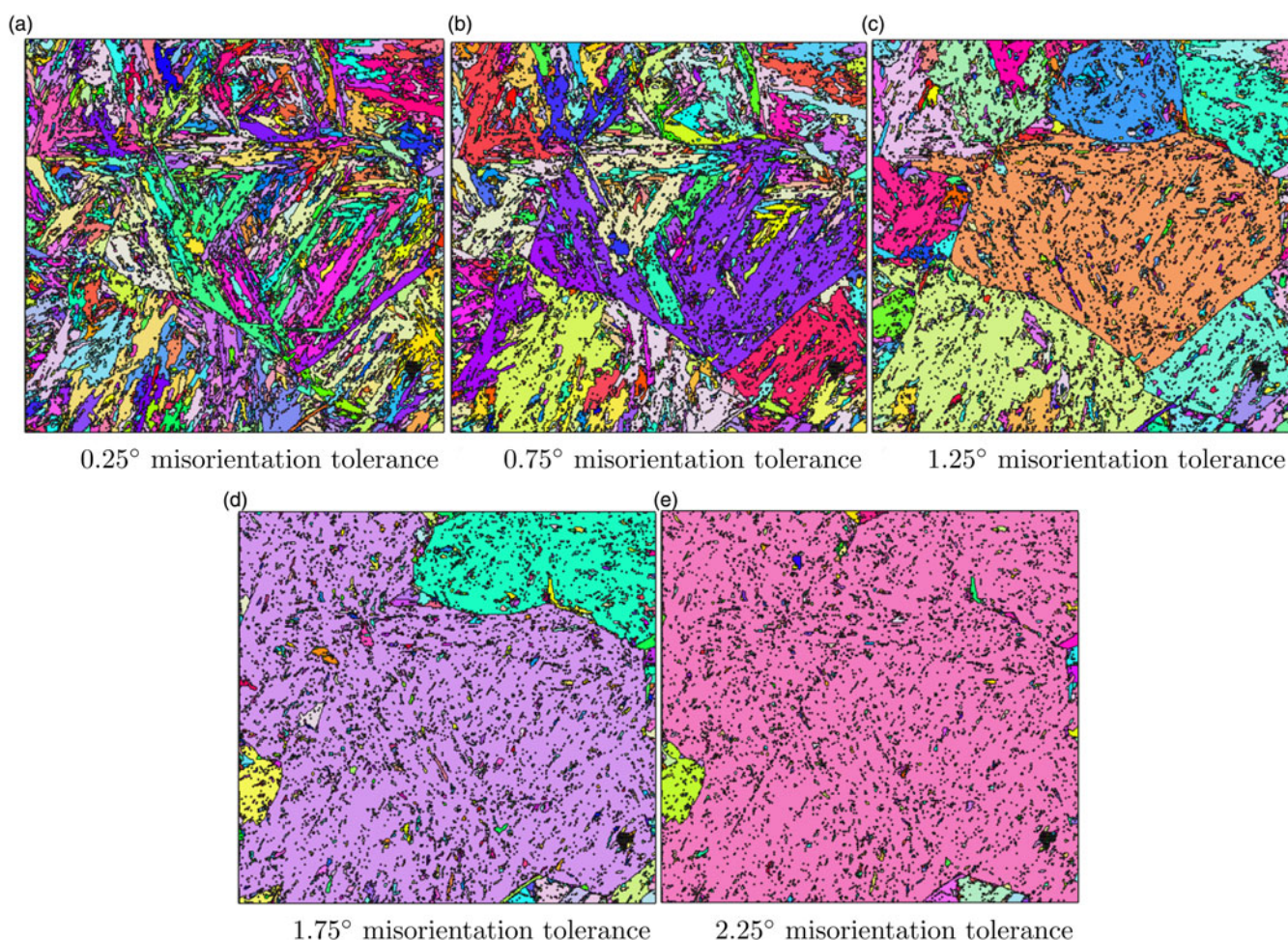
Fig. 8. Graph cut applied to segmentation of EBSD data from a multi-component steel microstructure (a) using IQ (b) and KAM map data (c). In (d), red corresponds to ferrite, blue corresponds to bainite, and green corresponds to martensite regions.

atoms are more likely to come from the more densely populated regions and background atoms should fall within the sparser regions:

$$w^{OP}(v^{(i)}, v^{(j)}) = f(w^{IP}(v^{(i)}, v^{(j)})|\{\mu_\eta, \sigma_\eta\})$$

$$= \alpha_\eta \left(\frac{1}{\sigma_\eta \sqrt{2\pi}} \exp \left(\frac{-(w^{IP}(v^{(i)}, v^{(j)}) - \mu_\eta)^2}{2\sigma_\eta^2} \right) + \omega_\eta \right)$$

$$(15)$$

Here, η refers to either a background or clustered designation for each respective atom and α and ω are equivalent to the parameters found in equation (6).

Cuts were then performed on a per-atom basis, where the technique only extracted nodes that were identified as residing within a cluster. In total, 10 clusters of 100 atoms each were created and distributed randomly throughout the background. This resulted in 1,000 total clustered atoms, which remained static throughout the analysis. The number of background atoms was increased dramatically, from a 1:1 ratio of 2,000 total atoms to a 50:1 ratio of 51,000 atoms in order to test the efficacy of the algorithm in the face of increasing noise (background atoms), hindering the ocular distinction of clusters within the dataset. The

generated cuts for varied ratios of background-to-clustered atoms can be seen below in Figure 10:

As Figure 10 details, the algorithm does an excellent job of identifying the locations of the clusters for relatively noisy datasets, even if the denoted clusters are denser than the actual synthetic cluster. In the 50:1 background:cluster (BG:C) case, displayed in Figure 10d, even picking out the clusters by eye is nearly impossible. However, the graph cut adequately captures the locations of clusters, albeit with some additional noise and some smaller faux-clusters. The number of identified clusters remains consistent and accurate up to a 10:1 ratio, with a small, additional noisy cluster generated in the 20:1 case. The scaling parameters of α for each respective case are given below in Table 3, as ω for both cluster and background atom pairings was 0.

We also wanted to test the algorithm against increasingly sparse clusters to see how dense the clusters need to be for sufficient results. To achieve this, the 10:1 ratio dataset was chosen and atoms from each cluster were iteratively redistributed into the background. This not only increases the BG:C atomic ratio, but it also decreases the density of each respective cluster, effectively making it more difficult to probabilistically define the likelihood that certain locations contained clusters or not. The results are displayed in Figure 11.

As the number of displaced clustered atoms reaches around 50% (Fig. 11d), diminishing the number of atoms from each
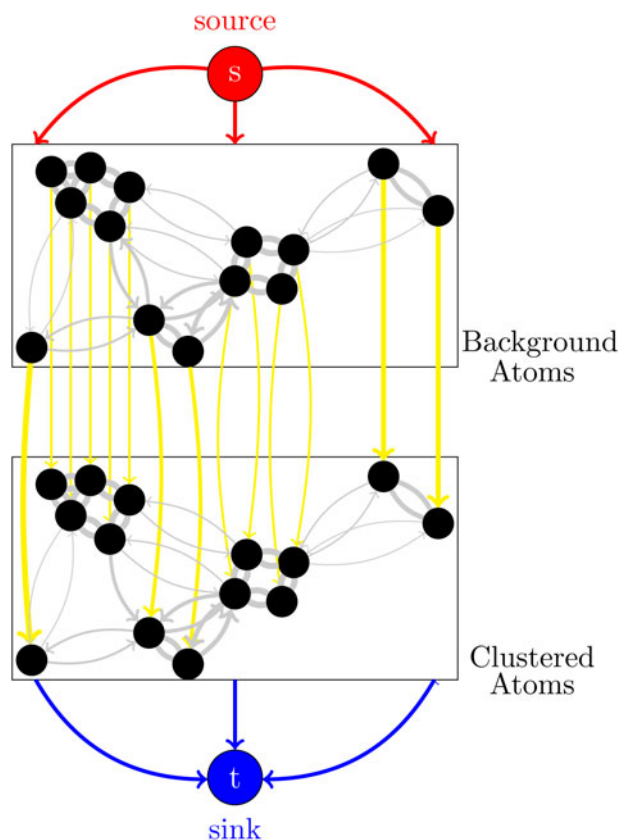
Fig. 9. Segmentation of austenite grain from martensitic steel EBSD dataset. The color key in (a) is identical to that for the EBSD data in Figure 8a.

cluster down to 50, the algorithm does a decent job of identifying the clustered locations. Furthermore, the number of atoms flagged as a cluster is limited, even as the density of each respective cluster is decreased dramatically. Although the edges show an increasing amount of noise with each additive displacement of clustered atoms, the amount of noise contained within the middle of the dataset remains low, and 10 clusters are recognized by the graph-cutting technique for each given case. The number of atoms within every cluster for each displacement iteration can be seen below in Table 4.

Although the algorithm tends to add atoms to each cluster, the results are promising and would suggest further development of the model to obtain more accurate and consistent results. Again, ω was 0 for each specific case, and Table 5 details the scaling parameters for α for both background and cluster designations.

Finally, a modified *k*-means approach (Lloyd, 1982) was implemented as a rudimentary comparison to the presented graph cutting approach using the built-in MATLAB function. Since the datasets are synthetic and therefore the number of clusters was known a priori, the number of clusters to identify was automatically set to 10 to optimize results. Additionally, the distance between each atom and the central point for each determined cluster was also computed. However, considering the function only groups the atoms into corresponding clusters without exclusion, there would be no atoms flagged as having come from the background. To rectify this, a tolerance was added that compared the distance of an atom's location with that of its nearest cluster's central point. If the distance exceeded the tolerance, the atom was rejected from the cluster and re-indexed as a

background atom. This tolerance was then adjusted until the most reasonable results were established for the first two cases in Figure 10 from the graph cutting technique. The latter cases, of a 20:1 and 50:1 background to cluster ratio break down and thus do not need to be shown. The background atomic arrangement fluctuates from those presented in the graph cutting case but the clustered atomic positions are equivalent. The results are presented below in Figure 12 along with the optimized tolerance values:

Discussion

The above examples demonstrate that our proposed graph-cutting framework can be used for a wide range of segmentation and clustering problems across a spectrum of input data types that commonly arise in advanced materials characterization. The main advantage of the graph-cut framework is the ease at which complex regularized optimization problems can be posed and subsequently solved. The graph structure itself gives a visual interpretation of the problem which aids in formulation. When developing the case studies presented above, the authors were surprised that often naive or "first-stab" ideas worked nearly as well as specialized algorithms such as EM/MPM (Comer & Delp, 2000). This strongly suggests that if paired with a well thought out graphical user interface, the method could be developed into a robust and user friendly materials data analysis tool and be integrated with commercial and open source image analysis tools such as BlueQuartz Software LLC, MIPAR (Sosa et al., 2014), Thermo Scientific™ pace Amiro-Avizo Software, MATLAB's Image Processing Toolbox™, etc. when a physically consistent, Bayesian-based setup is formulated. The first three problems involved a hasty the model layout to determine the effectiveness of the technique and whether it could be used to approach those specific problems. As such, enhanced refinement of the existing setups would most likely capture the desired information more effectively. However, the goal of the paper was to present a new methodology for approaching ill-defined inverse problems so long as a clear, inter-connected network of spatially resolved nodes could be established. The results suggest that the graph-cutting technique, with its diversity and accessibility, is a tantalizing approach that could be easily applied to these problems, as well as other similar ones in materials science.

For the specific example of image segmentation of γ' particles, there are clear issues with particle separation for all three tested methods, as some particles with a small separation between each other get lumped together into one large particle. However, the relative location and geometry of most of the particles are captured with a reasonably high signal-to-noise ratio. Compared with the EM/MPM technique, graph cutting results in a significantly less noisy image with improved particle attributes. The Otsu threshold method is slightly better at segmenting images with a large contrast between particles and matrix, as seen with the René 88 DT dataset. However, when more complicated images with less contrast need to be segmented, such as with the René 104 dataset, the graph cut segmentations contained the most geometrically accurate particles with the least amount of noise. This is because the intra-particle intensity gradients within the larger particles can be regularized with the graphcutting technique based on adjacent-pixel intensity values. A wider variety of images would need to be tested to most thoroughly test the efficacy of the three methods, but the examples here demonstrate graph cutting technique as a viable option for image segmentation in materials science applications.
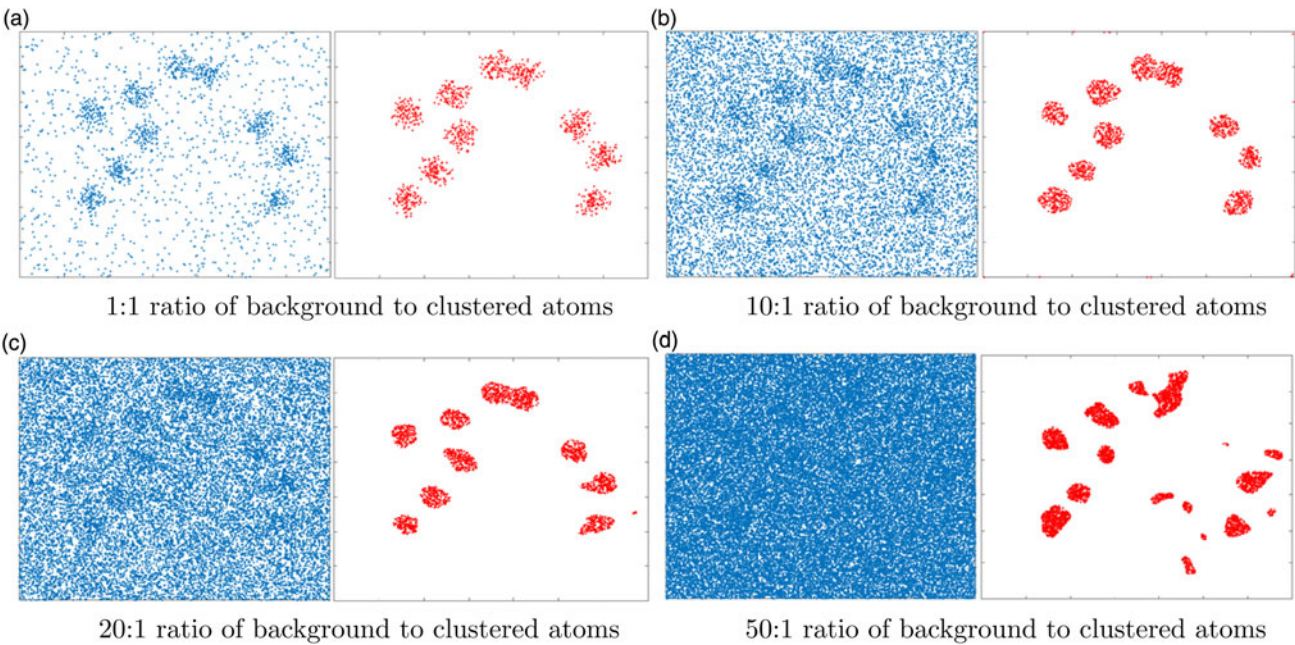
Fig. 10. Grain boundary misorientation austenite reconstructions performed using MTEX (Bachmann et al., 2010) for three separate angular tolerances: 0:25° (upper left), 1:25°, and 2:25° (right).

Table 3. Scaling Parameters Corresponding to the Cases Displayed in Figure 10, where Subscript BG Represents Favoring Background Atom Designation and C is Related to Clusters.

| BG:C Atomic Ratio	α_{BG}	α_C
1:1	1.6×10^4	5.0×10^0
10:1	3.9×10^5	3.1×10^3
20:1	7.8×10^4	1.6×10^4
50:1	2.0×10^6	2.5×10^1

With respect to microstructure constituent segmentation in hyperspectral data, the results show that the graph-cutting technique produces reasonable results, albeit without ground-truth validation. The determined location of the ferrite and bainite, clustered together and occupying points of high-IQ values, makes logical sense and is visually consistent with the IQ map. Additionally, the ability to produce repeatable results in the presence of excessive noise is a strong indicator of the robustness of the approach. Reproducibility suggests that a statistical test might be developed to determine the accuracy of the segmentation when results across a large number of EBSD scans are considered that could possibly distinguish between constituents could also be used to help classify the data, highlighting the versatility of the graph-cutting technique. This is especially evident when consideration of the cutting process is taken. Through the separation of the ferrite from the bainite/martensite mixture and consequent indexing of the latter, an instantaneous redistribution of spatial nodes occurs without user intervention, all corresponding to the constituent mixture. The resultant graph cut is only performed on these points, suggesting that this process could be repeated until no more nodes remain in the sink. Considering the KAM distributions between bainite and martensite are so similar, there could be a better approach to the segmentation that the authors have not presently thought of. Needless to say, the ease

with which these values can be computed from experimental data makes them alluring for this technique. More samples and validation would ultimately be required to fully endorse graph cutting in solving microstructure constituent segmentation, but the results seem promising.

As mentioned previously, the motivating application for the graph-cut technique was the analysis of transformation microstructure, particularly the identification of prior-transformation grains. This example study shows the limited case of identifying the points associated with a single prior-austenite grain given a reasonable estimate of the orientation. One can imagine an iterative search over the orientation space to identify the remainder of the grains and complete the reconstruction. However, specification and implementation of a complete and robust algorithm are well beyond the scope of this work. Here, the intention is simply a demonstration of how flexible the graph-cut approach is with respect to the data used to formulate the fidelity and penalization terms and to highlight an example that is outside the general set of problems associated with segmentation. When compared with the grain boundary misorientation tolerance approach, which is similar in nature to a flood fill inspired algorithm, we can see where the limitations exist. Too low of a misorientation tolerance identifies most martensite features as their own PAGs. Too high of a tolerance results in clustering the martensite features into a single, giant PAG. Even with the moderate tolerance that produces quasi-reasonable results, we can see the grains, most notably the large, centralized one we segment using the graph-cutting technique, is littered with noise and regions extend across the presumed boundaries.

Atom clustering segmentation showed sufficiently good results when being solved by graph cutting. As the density of the background atoms was increased, the density of the clusters increased as well. There seems to be no way around this, but the algorithm did work well for identifying possible nucleation sites in spite of high levels of noise. The noisy edges incorrectly flagged as clusters when the atoms were being displaced from the clusters may be the
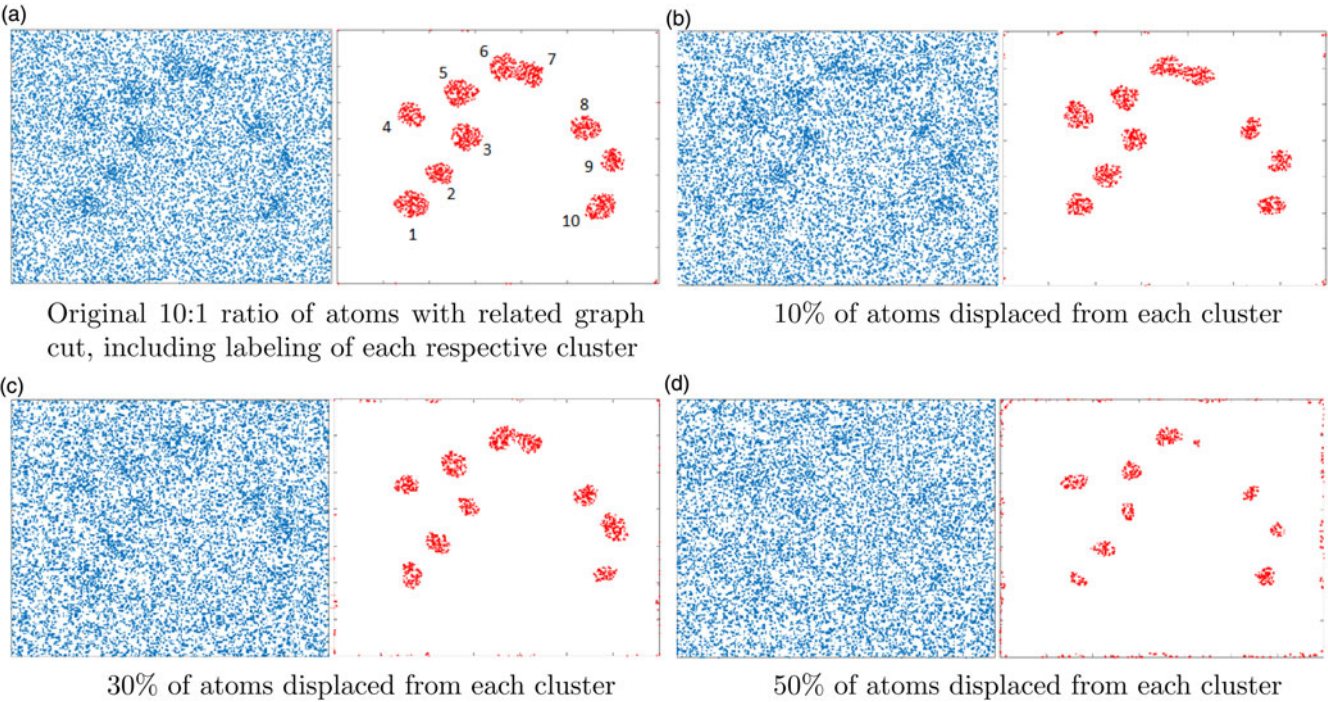
Fig. 11. Performance of graph cuts when removing clustered atoms and randomly dispersing them throughout the background. The number of clusters is consistent with those denoted in Table 4.

Table 4. The Percentage of Atoms Removed from Each Synthetic Cluster and Dispersed within the Background Compared with the Amount of Flagged Atoms in Each Cut Cluster for the 10:1 BG:C Ratio.

Cluster Label (%)	1	2	3	4	5	6	7	8	9	10
0	168	142	168	180	162	147	220	179	142	133
10	128	108	107	118	100	107	149	105	111	143
30	125	133	86	94	126	113	132	73	84	91
50 [a]	58	74	105	91	88	79	104	25	87	114

[a]Additional cluster containing 5 atoms.

Table 5. Scaling Parameters Corresponding to Figure 10, where Atoms were Randomly Displaced from Clusters and Added to the Background.

% of Displaced Atoms	α_{BG}	α_C
0	3.9×10^5	3.1×10^3
10	1.6×10^4	6.3×10^2
30	2.0×10^6	7.8×10^4
50	3.9×10^5	3.1×10^3

result of those atoms having fewer nearest neighbors, thereby resulting in skewed neighboring distances and increasing the likelihood that they came from clusters. This issue could possibly be prevented through the addition of a periodic boundary condition or mirrored interfaces, where a spatial pseudo-distribution of atoms with similar density to the dataset surrounding the atoms would increase the edge atoms nearest neighbor count and thus classify them as probabilistically more likely to have come from the background. The ability to characterize clusters even when the atoms are not as locally concentrated would be a considerable gain with respect to the analysis of APT data. In comparison to the k-means algorithm, which determines centrally located points around presumed clusters, our results show a much better ability at accurately identifying the location of clusters. Although the presented k-means the technique is not considered state of the art, the vast difference in reconstruction results suggests that the graph-cutting approach is a prospective new approach to atomic cluster segmentations from APT data. The next step would be to compare the results with some of the more established clustering algorithms to see how the graph cut technique manages.

Conclusions

In conclusion, graph cutting is a powerful technique that can be used to efficiently and effectively solve inverse problems efficaciously. The results for problems in image segmentation, microstructure constituent segmentation, parent grain segmentation applied to the $\gamma \rightarrow \alpha'$ transformation and atomic clustering identification are promising, suggesting that the technique can be used to handle difficult analysis issues within the computational materials science community. Implementation of models is simple,
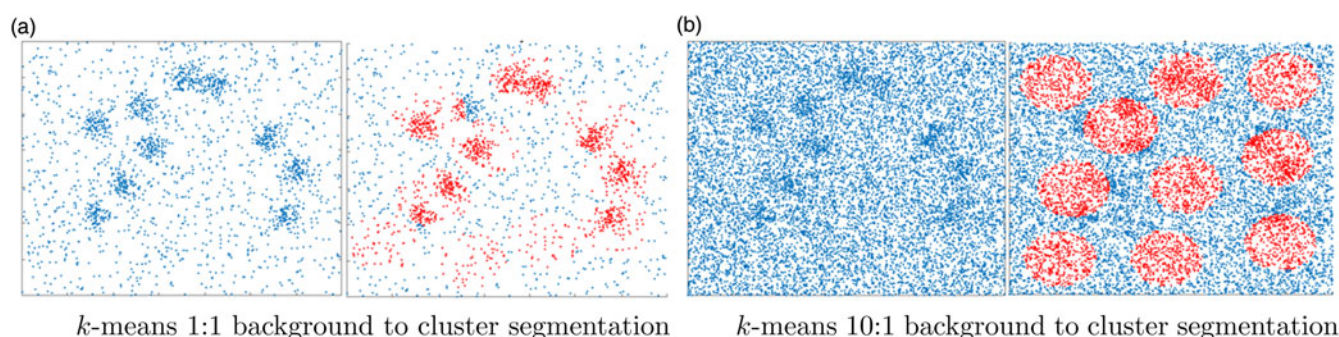
Fig. 12. The k-means segmentations for the graph cut cases represented in Figure 10 with relative distance tolerances of 0.025 and 0.025 for the 1:1 and 10:1 background to cluster ratio, respectively.

relying upon *Bayesian* statistical methods that can produce desirable results in the face of high levels of noise. Basing assumptions in probabilistic terms allows for a quantitative analysis of the results. Validation using experimental techniques would help bolster the approaches taken to solve each problem, and more profound models would only serve to improve upon results. The versatility of the technique suggests that more problems could be solved so long as effective networks of nodes can be established, including possible approaches to problems in diffusion, grain growth, recrystallization, and characterization of stress gradients within grains.

References

Abbasi M, Nelson T, Sorensen C & Wei L (2012). An approach to prior austenite reconstruction. *Mater Charact* **66**, 1–8.

Artan Y (2011). Interactive Image Segmentation Using Machine Learning Techniques, 2011 *Canadian Conference on Computer and Robot Vision*, 264–269.

Bachmann F, Hielscher R & Schaeben H (2010). Inferential statistics of electron backscatter diffraction data from within individual crystalline grains. *J Appli Crys* **43**, 1338–1355.

Bae E, Shi J & Tai X (2011). Graph cuts for curvature based image denoising. *IEEE Trans Image Process* **20**, 1199–1210.

Banerji S, McMahon CJ, J & Feng H (1978). Intergranular fracture in 4340-type steels: Effects of impurities and hydrogen. *Metall Trans A* **9A**, 237–247.

Beheshti M, Faichney J & Gharipour A (2015). Bio-Cell Image Segmentation using Bayes Graph-Cut Model.

Bernier N, Bracke L, Malet L & Godet S (2014). An alternative to the crystallographic reconstruction of austenite in steels. *Mater Charact* **89**, 23–32.

Bovik A (2000). *Handbook of Image and Video Processing*. New York: Academic.

Boykov Y & Kolmogorov V (2004). An experimental comparison of Min-Cut/Max-flow algorithms for energy minimization in vision. *IEEE Trans Pattern Anal Mach Intell (PAMI)* **26**, 1124–1137.

Boykov Y & Veksler O (2006). *Graph Cuts in Vision and Graphics: Theories and Applications*, In Paragios N, Chen Y & Faugeras O (eds), Handbook of Mathematical Models in Computer Vision. Boston, MA: Springer.

Brust A, Niezgoda S, Yardley V & Payton E (2019). Analysis of misorientation relationships between austenite parents and twins. *Metall Mater Trans A* **50**, 837–855.

Campbell A, Murray P, Yakushina E, Marshall S & Ion W (2018). New methods for automatic quantification of microstructural features using digital image processing. *Mater Des* **141**, 395–406.

Cayron C (2007). ARPGE: A computer program to automatically reconstruct the parent grains from electron backscatter diffraction data. *J Appl Crystallogr* **40**, 1183–1188.

Chan R, Ho C & Nikolova M (2005). Salt-and-pepper noise removal by median-type noise detectors and detail-preserving regularization. *IEEE Trans Image Process* **14**, 1479–1485.

Chuang H & Comer M (2010). A New Method for Segmentation of Noisy, Low-Contrast Image Sequences. *Processions on IEEE International Conference on Circuits and Systems*.

Cluff S, Nelso T, Song R & Fullwood D (2018). Crystallographic reconstruction of parent austenite twin boundaries in a lath martensitic steel. *Int Conf Ser: Mat Sci Eng* **375**, 1–11.

Comer M & Delp E (1994). Parameter Estimation and Segmentation of Noisy or Textured Images Using the EM Algorithm and MPM Estimation. *IEEE International Conference on Image Processing*, 650–654.

Comer M & Delp E (2000). The EM/MPM algorithm for segmentation of textured images: Analysis and further experimental results. *IEEE Trans Image Process* **9**, 1731–1744.

Cook WJ, Cunningham WH, Pulleyblank WR & Schriver A (1998). *Combinatorial Optimization*. New York: John Wiley & Sons.

Davies R (1978). Influence of martensite composition and content on the properties of dual phase steels. *Metall Trans A* **9**, 671–679.

Despotović I, Jelač V, Vansteenkiste E & Philips W. (2010). Noise-Robust method for image segmentation. International Conference on Advanced Concepts for Intelligent Vision Systems, Springer, Berlin, Heidelberg, Dec 13, 2010. pp. 153–162.

Duval L, Moreaud M, Couprie C, Jeulin D, Talbot H & Angulo J (2014). Image processing for materials characterization: Issues, challenges and opportunities, 2014. *IEEE International Conference on Image Processing (ICIP)*, 4862–4866.

El-Bagoury N & Mohsen Q (2011). Gamma prime and TCP phases and mechanical properties of thermally exposed nickel-base superalloy. *Phase Transitions* **84**, 1108–1122.

Faessel M & Jeulin D (2010). Segmentation of 3D microtomographic images of granular materials with the stochastic watershed. *J Microsc* **239**, 17–31.

Felfer P, Ceguerra A, Ringer S & Cairney J (2015). Detecting and extracting clusters in atom probe data: A simple, automated method using voronoi cells. *Ultramicroscopy* **150**, 30–36.

Ford L & Fulkerson D (1962). *Flows in Networks*. Princeton, NJ: Princeton University Press.

Girault E, Jacquest P, Harlet P, Mols K, Humbeeck JV, Aernoudt E & Delannay F (1998). Metallographic methods for revealing the multiphase microstructure of TRIP-assisted steels. *Mater Charact* **40**, 111–118.

Gnäupel-Herold T & Creuziger A (2011). Diffraction study of the retained austenite content in TRIP steels. *Mater Sci Eng: A* **528**, 3594–3600.

Goldberg A & Tarjan R (1988). A new approach to the maximum-flow problem. *J Assoc Comp Mach* **35**, 921–940.

Greig D, Porteous B & Seheult A (1989). Exact Maximum A posteriori estimation for binary images. *J Roy Stats Soc* **51**, 271–279.

Greninger AB & Troiano AR (1949). The mechanism of martensite formation. *Metals Transactions* **185**, 590–598.

Hata K, Wakita M, Fujiwara K & Kawano K (2017). Development of a Re-construction method of prior austenite microstructure using EBSD data of martensite. *Nippon Steel and Sumitomo Metal Technical Report* **114**, 26–31.

Heimann T & Meinzer H (2009). Statistical shape models for 3D medical image segmentation: A review. *Med Image Anal* **13**, 543–563.

Hong S & Yu J (1989). Effect of prior austenite grain size on creep properties and on creep crack growth in 3.5-Ni-Cr-Mo-V steel. *Scr Mater* **23**, 1057–1062.

Horn R & Ritchie R (1978). Mechanisms of tempered martensite embrittlement of low alloy steels. *Metall Trans A* **9A**, 1039–1053.

Hutchinson B, Ryde L, Lindh E & Tagashira K (1998). Texture in hot rolled austenite and resulting transformation products. *Mater Sci Eng A* **257**, 9–17.

Hyde J & English C (2000). An Analysis of the Structure of Irradiation Induced Cu-Enriched Clusters in Low and High Nickel Welds. *Symposium of Microstructural Processes in Irradiated Materials*, 27–30.

Imre E, Guillemaut JY & Hilton A (2010). Moving Camera Registration for Multiple Camera Setups in Dynamic Scenes. *Proceedings of the British Machine Vision Conference*, 38.1–38.12, BMVA Press.

Iyer G, Chanussot J & Bertozzi A (2017). A graph-based approach for feature extraction and segmentation of multimodal images, 2017. *IEEE International Conference on Image Processing* (ICIP), 3320–3324.

Johansen T (1997). On Tikhonov regularization, bias and variance in nonlinear system identification. *Automatica* **33**, 441–446.

Kang J, Kim D, Baik S, Ahn T, Kim Y, Han H, Oh K, Lee H & Han S (2011). Phase analysis of steels by grain-averaged EBSD functions. *Iron Steel Inst Japan Int* **51**, 130–136.

Keller R, Roshko A, Geiss R, Bertness K & Quinn T (2004). EBSD measurement of strains in GaAs due to oxidation of buried AlGaAs layers. *Microelectron Eng* **75**, 96–102.

Kelly P, Jostons A & Blake R (1990). The orientation relationship between lath martensite and austenite in low carbon, low alloy steels. *Acta Metall Mater* **38**, 1075–1081.

Kimura K, Ohi N, Shimazu K & Matsuo T (1987). Effect of prior austenite grain size on high temperature creep properties of Cr-Mo-V rotor steel. *Scr Mater* **21**, 19–22.

Kitahara H, Ueji R, Tsuji N & Minamino Y (2006). Crystallographic features of lath martensite in low-carbon steel. *Acta Mater* **54**, 1279–1288.

Kurdjumow G & Sachs G (1930). Ü ber der Mechanismus der Stahlhärtung (On the mechanism of hardening of steel). *Z Physik* **64**, 325–343.

LaPera F (1978). Improved etching technique for the determination of percent martensite in high-strength, dual-phase steels. *Metallography* **12**, 263–268.

Lee C & Han J (2013). Learning Markov Random Field Image Prior for Pixelation Removal of Fiber Microscopy Using Sparse Coding Based on Bayesian Framework. *International Winter Workshop on Brain-Computed Interface* (BCI).

Leskó M, Kato Z & Nagy A (2010). Live Cell Segmentation in Fluorescence Microscopy via Graph Cut, 1485–1488.

Lloyd S (1982). Least squares quantization in PCM. *IEEE Trans Inf Theory* **28**, 129–137.

MacSleyne J, Uchic M, Simmons J & Graef MD (2009). Three-dimensional analysis of secondary γ' precipitates in René-88 DT and UMF-20 superalloys. *Acta Mater* **57**, 6251–6267.

Marroquin J, Mitter S & Poggio T (1987). Probabilistic solution of Ill-posed problems in computational vision. *J Am Stats Assoc* **82**, 76–89.

McInerney T & Terzopoulos D (1999). Topology adaptive deformable surfaces for medical image volume segmentation. *IEEE Trans Med Imaging* **18**, 840–850.

Mondal P, Vicidomini G & Diaspro A (2007). Markov random field aided Bayesian approach for image reconstruction in confocal microscopy. *J Appl Phys* **102**, 044701.

Morito S, Tanaka H, Konishi R & Maki T (2003). The morphology and crystallography of lath martensite in Fe-C alloys. *Acta Mater* **51**, 1789–1799.

Neubauer A (1989). Tikhonov regularisation for non-linear ill-posed problems: Optimal convergence rates and finite-dimensional approximation. *Inverse Prob* **5**, 541–557.

Otsu N (1979). A threshold selection method from gray-level histograms. *IEEE Trans Syst* **9**, 62–66.

Payton E, Aghajani A, Otto F, Eggler G & Yardley V (2012). On the nature of internal interfaces in a tempered martensite ferritic steel and their evolution during long-term creep. *Scr Mater* **66**, 1045–1048.

Payton EJ & Nolze G (2013). The backscatter electron signal as an additional tool for phase segmentation in EBSD. *Microsc Microanal* **19**, 929–941.

Payton EJ, Phillips PJ & Mills MJ (2010). Semi-automated characterization of the gamma prime phase in Ni-based superalloys via high-resolution backscatter imaging. *Mater Sci Eng A* **527**, 2684–2694.

Payton EJ, Phillips PJ & Mills MJ (2011). Stereology of backscatter electron images of etched surfaces for characterization of particle size distributions and volume fractions: Estimation of imaging bias Via monte carlo simulations. *Mater Charact* **62**, 563–574.

Petrov R, Kestens L, Wasilkowska A & Houbaert Y (2007). Microstructure and texture of a lightly deformed TRIP-assisted steel characterized by means of the EBSD technique. *Mater Sci Eng A* **447**, 285–297.

Poggio T, Voorhees H & Yuille A (1988). A regularized solution to edge detection. *J Complex* **4**, 106–123.

Preethi S & Narmadha D (2012). A survey on image denoising techniques. *Int J Comput Appl* **58**, 27–30.

Ramírez A, Porcayo-Calderon J, Mazur Z, Salinas-Bravo V & Martinez-Gomez L (2016). Microstructural changes during high temperature service of a cobalt-based superalloy first stage nozzle. *Adv Mater Sci Eng* **2016**, 1–7.

Rodríguez P (2013). Total variation regularization algorithms for images corrupted with different noise models: A review. *J Elect Comput Eng* **2013**, 1–18.

Sandvik B & Wayman C (1983). Characteristics of lath martensite: Part 1. Crystallographic and substructural features. *Metallurgical Transactions: A* **14A**, 809–822.

Shibata A, Morito S, Furuhara T & Maki T (2009). Substructures of lenticular martensites with different martensite start temperatures in ferrous alloys. *Acta Mater* **57**, 483–492.

Shigeta H, Mashita T, Kaneko T, Kikuta J, Senoo S, Takemura H, Matsuda H & Ishii M (2014). A Graph Cuts Image Segmentation Method for Quantifying Barrier Permeation in Bone Tissue, 16–19.

Shinozaki T, Nakanishi T, Suzuki K & Miura H (2016). Measurement of the strength of a grain boundary in electroplated copper thin-film interconnections by using micro tensile-test, 2016. *IEEE 37th International Electronics Manufacturing Technology* (IEMT) 18th *Electronics Materials and Packaging* (EMAP) Conference, 1–5.

Simmons J, Chuang P, Comer M, Spowart J, Uchic M & Graef M (2009). Application and further development of advanced image processing algorithms for automated analysis of serial section image data. *Mod Sim Mat Sci Eng* **17**, 1–22.

Soni M, Khare A & Jain S (2014). Problem of denoising in digital image processing and its solving techniques. *Int J Emerging Technol Adv Eng* **4**, 244–250.

Sosa JM, Huber DE, Welk B & Fraser HL (2014). Development and application of MIPAR$_t$ m : A novel software package for Two- and three-dimensional microstructural characterization. *Integrating Mat Manuf Innovation* **3**, 10.

Soubies E, Weiss P & Descombes X (2015). *Graph Cut Based Segmentation of Predefined Shapes: Applications to Biological Imaging*, In Fred A & De Marsico M (eds), Pattern Recognition Applications and Methods. Advances in Intelligent Systems and Computing, vol 318. Cham, Switzerland: Springer International Publishing. pp. 153–170.

Stephenson L, Moody M, Liddicoat P & Ringer S (2007). New techniques for the analysis of fine-scaled clustering phenomena within atom probe tomography (APT). *Microstruct Microanal* **13**, 448–463.

Tan W (2017). *Investigations of phase transformations in AISI 5160 steel and partially stabilized zirconia via electron backscatter diffraction based techniques*. PhD Thesis. Alfred University.

Tan W, Lipke D, Dziaszyk S & Payton E (2018). On Quantitatively Identifying Different Constituents in Multicomponent Steel Microstructures in EBSD, *Manuscript submitted for publication*.

Tibshirani R (1996). Regression shrinkage and selection via the LASSO. *J R Statistical Soc Ser B (Methodological)* **58**, 267–288.

Tolba A & Raafat H (2015). Multiscale image quality measures for defect detection in thin films. *Int J Adv Manuf Technol* **79**, 113–122.

Torre V & Poggio TA (1986). On Edge Detection. *IEEE Transactions on Pattern Analysis and Machine Intelligence* PAMI-8, 147–163.

Uchic M & MacSleyne J (2006). Ground Truth Segmentation Image, http://www.bluequartz.net/binaries/Data/Rene88DT-GT.zip, [Online; accessed 08-August-2018].

Veksler O (2003). Extracting dense features for visual correspondence with graph cuts, 2003. *IEEE Computer Society Conference on Computer Vision and Pattern Recognition, 2003. Proceedings*, vol. **1**, 1689–1694.

Waggoner J, Zhou Y, Simmons J, Graef MD & Wang S (2013). 3D materials image segmentation by 2D propagation: A graph-Cut approach considering homomorphism. *IEEE Trans Image Process* **22**, 5282–5293.

Waggoner J, Zhou Y, Simmons J, Graef MD & Wang S (2014). Graph-Cut based interactive segmentation of 3D materials-science images. *Mach Vis Appl* **25**, 1615–1629.

Wayman C (1975). Shear transformations and microstructure. *Metallography* **8**, 105–130.

Wills J, Agarwal S & Belongie S (2003). What went where [motion segmentation], *Computer Vision and Pattern Recognition, 2003. Proceedings. 2003 IEEE Computer Society Conference on*, vol. 1, I–I, IEEE.

Wright S, Nowell M & Fields D (2011). A review of strain analysis using electron backscatter diffraction. *Microsc Microanal* **17**, 316–329.

Wu J, Wray P, Garcia C, Hua M & DeArdo A (2005). Image quality analysis: A new method of characterizing microstructures. *ISIJ Int* **45**, 254–262.

Yardley V, Fahimi S & Payton E (2015). Classification of creep crack and cavitation sites in tempered martensite ferritic steel microstructures. *Mater Sci Technol* **31**, 547–553.

Yardley V, Payton E, Matsuzaki T, Sugiura Jr. R, Tsurekawa AY, S & Hasegawa Y (2012). EBSD analysis of creep cracking in a 12 wt.% Cr tempered martensite ferritic steel. *Proceedings of the 12th international conference on creep and fracture of engineering materials and structures, Kyoto, Japan*.

Zaefferer S, Romano P & Friedel F (2008). EBSD as a tool to identify and quantify bainite and ferrite in low-alloyed Al-TRIP steels. *J Microsc* **230**, 499–508.

Zelenty J, Dahl A, Hyde J, Smith G & Moody M (2017). Detecting clusters in atom probe data with Gaussian mixture models. *Microstruct Microanal* **23**, 269–278.

Zhang J, Modestino W & Langan D (1994). Maximum-Likelihood parameter estimation for unsupervised stochastic model-based image segmentation. *IEEE Trans. Image Process* **3**, 404–420.

Zhu Y, Wang A & Ma J (2013). Two-Phase image segmentation with the competitive learning based chan-vese (CLCV) model. In *Intelligent Computing Theories*, Huang D, Bevilacqua V, Figueroa J & Premaratne P (Eds.), pp. 183–191. Berlin, Heidelberg: Springer Berlin Heidelberg.